

Hydrodynamic correlations for bubble columns from complementary UXCT and RPT measurements in identical geometries and conditions

Azizi, S.; Yadav, A.; Lau, Y. M.; Hampel, U.; Roy, S.; Schubert, M.;

Originally published:

November 2019

Chemical Engineering Science 208(2019), 115099

DOI: <https://doi.org/10.1016/j.ces.2019.07.017>

Perma-Link to Publication Repository of HZDR:

<https://www.hzdr.de/publications/Publ-29616>

Release of the secondary publication
on the basis of the German Copyright Law § 38 Section 4.

CC BY-NC-ND

Hydrodynamic correlations for bubble columns from complementary UXCT and RPT measurements in identical geometry and conditions

S. Azizi^a, A. Yadav^b, Y.M. Lau^a, U. Hampel^{a,c}, S. Roy^b, M. Schubert^{a,1}

^a*Institute of Fluid Dynamics, Helmholtz-Zentrum Dresden-Rossendorf, Bautzner Landstraße 400, 01328 Dresden, Germany*

^b*Department of Chemical Engineering, Indian Institute of Technology-Delhi, Hauz Khas, New Delhi, Delhi 110016, India*

^c*Chair of Imaging Technologies in Energy and Process Engineering, Technische Universität Dresden, 01062 Dresden, Germany*

¹*Corresponding author: Email: m.schubert@hzdr.de (M. Schubert)*

Abstract

Many correlations have been developed to predict the hydrodynamics of bubble columns. Often, these studies are performed for incomparable systems in terms of column and sparger dimensions as well as physical fluid properties. In this work, a different approach is proposed comprising interrelated correlations for liquid velocity, gas holdup and bubble size. The correlations are developed on the basis of complementary experiments with non-invasive measurement techniques, namely, Ultrafast X-ray Computed Tomography (UXCT) and Radioactive Particle Tracking (RPT). The experimental setup consists of a bubble column equipped with a needle sparger. Developed correlations consider sparger dimensions, operating conditions and bubble size. The bubble size is applied as the characteristic length in the Reynolds and the Eötvös numbers, which are utilized for the gas holdup and liquid velocity correlations. In comparison with previous approaches, the developed correlations show better agreement with experimental data from this study as well as from the literature.

Keywords: Bubble columns, hydrodynamic correlations, ultrafast X-ray computed tomography, radioactive particle tracking

1. Introduction

A bubble column reactor is a widely applied equipment in the chemical industry due to its superior gas-liquid contacting ability, excellent mass and heat transfer performance, intensive mixing without moving parts and comparably low energy consumption (Dudukovic and Mills, 1984, Deen et al., 2010). The excellent mixing characteristics prevent the formation of temperature hotspots and thus, ensures high thermal stability. Despite the simple column design, the multiphase flow within is complex and the process design requires detailed knowledge on the key hydrodynamic properties, such as gas holdup, bubble size, liquid velocity and liquid circulation velocity (Shimada et al., 2012). For instance, the mass transfer rate of a chemical component into the liquid phase varies with the degree of liquid mixing due to the dependency of the mass transfer coefficient on bubble size, gas holdup, liquid velocity distribution and liquid circulation velocity (Levenspiel, 1999). Particularly, the coefficients of heat and mass transfer correlations rely strongly on the gas holdup (Letzel et al., 1999, Akita and Yoshida, 1973, Götz et al., 2017). The spatial variation of the gas holdup is intimately related to the

15 pressure gradients in the column cross-section, which in turn results in liquid circulation in the
bubble column and affect liquid mixing as well as heat and mass transfer (Letzel et al., 1999,
Kantarci et al., 2005). The specific gas-liquid interfacial area is an important design factor,
which directly correlates with the gas holdup and inversely with the bubble size. To enhance
the interfacial area for the gas-liquid mass transfer, small bubbles are desired (Polli et al.,
2002). As a consequence, smaller bubbles lead to higher gas residence time and higher gas
holdups (Letzel et al., 1999, Kantarci et al., 2005). In contrast, large bubbles experience large
net forces resulting from buoyancy and drag, which cause higher rise velocities. However, the
existence of large bubbles with high rising velocities causes increasing of liquid mixing, which
is desired for the increasing of heat transfer to immersed surfaces in the industrial bubble
25 columns. Another implication of the radial gas holdup distribution is the radial variation of
the liquid velocity. The liquid velocity distribution is important due to its particular effects on
the convective heat and mass transfer (Gandhi et al., 2009). Increasing the liquid circulation
velocity increases the liquid mixing in the bubble column, which causes a reduction of local
concentration gradients due to a higher mass transfer rate.

30 All these aforementioned parameters in bubble columns depend significantly on operating
conditions, liquid properties, column dimensions, gas distributor design, etc. (Letzel et al.,
1999, Kantarci et al., 2005). Subsequently, numerous correlations for bubble size, gas holdup,
and liquid velocity have been proposed. These correlations are either developed on the basis
35 of experiments from particular setups or different operating conditions. Although it is known
that bubble size, gas holdup, liquid velocity and mixing are not independent from each other
(Schafer et al., 2002, Basha et al., 2015, Sal et al., 2013), a complete experimental database to
derive the correlations for bubble size, gas holdup, and liquid velocity for identical bubble col-
umn geometry and operating conditions are, as far as the authors recalled, not yet compiled.
40 In this work, such a database is assembled on the basis of complementary experimental data
using Ultrafast X-ray Computed Tomography (UXCT) and Radioactive Particle Tracking
(RPT) for the derivation of hydrodynamic correlations. Contrary to literature correlations,
not only is this a unique concept, but also the developed correlations are “coupled” beside
dependency on physical properties, column dimensions and operating conditions. Starting
45 from the derivation of the inlet bubble size correlation, the mean bubble size correlation is
derived. Subsequently, the mean bubble size is applied as the characteristic length for the
dimensionless Reynolds and Eötvös numbers, which are utilized in the derivation of the gas
holdup and liquid velocity correlations. As such, the coupling is described as “one-way”.

50 In the following sections, literature correlations are revisited and the procedure of deriving
the hydrodynamic correlations is described. The employed state-of-the art measurement
techniques are presented for assembling a complementary experimental database. And finally,
the derived set of coupled correlations is given and its performance is compared with both
correlations and experimental data from literature.

55 2. Hydrodynamic correlations

Below, literature correlations are briefly listed for bubble size, gas holdup and liquid
velocity. Afterwards, the procedure for deriving hydrodynamic correlations is explained with
using complementary experimental data.

2.1. Bubble size

Table 1 shows correlations for the prediction of the initial bubble diameter, \bar{d}_i (bubble diameter at sparger), which is mostly described in terms of sparger orifice diameter, d_o (Leibson et al., 1956, Miller, 1974, Bhavaraju et al., 1978, Moo-Young and Blanch, 1981) and orifice superficial gas velocity, U_{go} (Leibson et al., 1956, Bhavaraju et al., 1978, Moo-Young and Blanch, 1981). Amongst these studies, only Bhavaraju et al. (1978) considered properties of the liquid phase instead of the gas phase. Beside these empirical correlations, Geary and Rice (1991) developed a model based on the force balance to predict the initial bubble diameter for rigid and flexible spargers.

Table 1: Correlations for the prediction of the initial bubble diameter.

Reference	Correlation
Leibson et al. (1956)	$\bar{d}_i = 0.18d_o^{1/2} \left(\frac{\rho_g U_{go} d_o}{\mu_g} \right)^{1/3}, \quad \frac{\rho_g U_{go} d_o}{\mu_g} < 2000$
Miller (1974)	$\bar{d}_i = \left(\frac{6\sigma d_o^{0.48}}{g(\rho_l - \rho_g)} \right)^{1/3}, \quad \text{for low gas flow rates}$
Bhavaraju et al. (1978)	$\bar{d}_i = 3.23d_o \left(\frac{\rho_l U_{go} d_o}{\mu_l} \right)^{-0.1} \left(\frac{\pi U_{go}^2 / 4}{d_o^3 g} \right)^{0.21}$
Moo-Young and Blanch (1981)	$\bar{d}_i = (0.19d_o^{0.48}) \left(\frac{\rho_g U_{go} d_o}{\mu_g} \right)^{0.32}$
Geary and Rice (1991)	$y = \frac{\bar{d}_i^3}{d_o^3}$ $\frac{0.5g(d_i^3/6)^2}{11d_o(d_o^2 U_{go})^2}(y^2 - 1 - 2\ln y) + N_r(y - 1 - \ln y) - 2 - N_\mu(2(y^{1/2} - 1) - \ln y) -$ $\frac{2(\pi d_i^3/6)^{1/3}}{d_o} \left(\frac{1}{36\pi} \right)^{1/3} (3(y^{1/3} - 1) - \ln y) = 0$ $N_r = \frac{32}{11} \frac{\pi d_i^3/6}{\rho_l (\pi d_o^2 U_{go}/4)^2 d_o} \left(\frac{\pi d_o^2 U_{go}^2 \rho_g}{4} - \pi \sigma d_o \right)$ $N_\mu = \frac{128}{11} \frac{5\sqrt{\pi d_i^3/6}}{d_o^3 U_{go}} \sqrt{\frac{2\mu_l}{\rho_l}} \left(\frac{d_o^2 U_{go}}{16} \right)^{3/2} \left(\frac{4\pi}{3} \right)^{1/2}$

The inlet bubble does not retain its initial bubble size due to breakup and coalescence events that changes the bubble size along its rising path. Considering the variety of breakup and coalescence models (Liao and Lucas, 2009, 2010), uncertainties of model coefficients and the complexity of the population balance equations, simplified empirical correlations are needed for the assessment of the bubble diameter. Table 2 shows correlations for the prediction of the mean bubble diameter, \bar{d}_m in bubble columns. Krishna et al. (1991) and Krishna and

Table 2: Correlations for the prediction of the mean bubble diameter.

Reference	Correlation
Krishna and Ellenberger (1996)	$\bar{d}_{mL} = \alpha_1(U_g - U_{df})^{2/5}(0.03 + h^*)^{4/5}g^{-1/5}$ $U_{df} = \frac{1}{2.84} \frac{\sigma^{0.12}}{\rho_g^{0.04}} \bar{\alpha}_{gm,trans} (1 - \bar{\alpha}_{gm,trans})$ $\bar{\alpha}_{gm,trans} = 0.59 \times 3.85^{1.5} \sqrt{\frac{\rho_g^{0.96} \sigma^{0.12}}{\rho_l}}$ $\bar{d}_{mS} \text{ not reported}$
Akita and Yoshida (1973)	$\bar{d}_m = 26D \left(\frac{D^2 g \rho_l}{\sigma} \right)^{-0.5} \left(\frac{U_g D^3 \rho_l^2}{\mu_l^2} \right)^{-0.12} \left(\frac{U_g}{\sqrt{gD}} \right)^{0.12}$
Wilkinson et al. (1994)	$\bar{d}_m = (8.8 \frac{\sigma}{\rho_l g})^{0.5} \left(\frac{U_g \mu_l}{\sigma} \right)^{-0.04} \left(\frac{\sigma^3 \rho_l}{g \mu_l^4} \right)^{-0.12} \left(\frac{\rho_l}{\rho_g} \right)^{0.22}$
Jamialahmadi et al. (2000)	$\bar{d}_i = \left(\frac{6\sigma d_o^{0.48}}{g(\rho_l - \rho_g)} \right)^{1/3}$ $\bar{d}_t = 0.45 U_g^{0.87} \alpha_g^{0.85}$ $\bar{d}_m = \sqrt[3]{\bar{d}_i^3 + \bar{d}_t^3}$
Kumar et al. (1976)	$\bar{d}_m = \begin{cases} 1.56 \left(\frac{\rho_g U_{go} d_o}{\mu_g} \right)^{0.058} \left(\frac{\sigma d_o^2}{(\rho_l - \rho_g) g} \right)^{0.25} & 1 < \frac{\rho_g U_{go} d_o}{\mu_g} < 10 \\ 0.32 \left(\frac{\rho_g U_{go} d_o}{\mu_g} \right)^{0.425} \left(\frac{\sigma d_o^2}{(\rho_l - \rho_g) g} \right)^{0.25} & 10 < \frac{\rho_g U_{go} d_o}{\mu_g} < 2100 \\ 100 \left(\frac{\rho_g U_{go} d_o}{\mu_g} \right)^{-0.4} \left(\frac{\sigma d_o^2}{(\rho_l - \rho_g) g} \right)^{0.25} & 4000 < \frac{\rho_g U_{go} d_o}{\mu_g} < 70000 \end{cases}$

Ellenberger (1996) described \bar{d}_m per class of their two-bubble class model for the churn-turbulent flow, i.e. large and small bubble classes. In the two-bubble class model, Krishna and Ellenberger (1996) proposed a correlation for the large bubble diameter, \bar{d}_{mL} , which depends on the gas holdup at flow regime transition. However, they did not consider a correlation for the diameter of the small bubbles, \bar{d}_{mS} . Others simply just use the mean bubble diameter of the whole bubbly flow. The correlations predicting bubble sizes show an increase with increasing of superficial gas velocity (Akita and Yoshida, 1973, Basha et al., 1976).

2015, Kantarci et al., 2005), surface tension and viscosity (Kantarci et al., 2005, Akita and Yoshida, 1973). Contrary, elevated pressure and increasing gas density reduce the mean bubble size (Wilkinson et al., 1994). The effect of temperature is ambiguous and depends on the non-linear change of vapor pressure, liquid viscosity and surface tension (Wilkinson et al., 1994). However, the inconsistent predictions of the bubble size can be attributed to the respective database gathered for different physical properties, operating conditions, column dimensions and sparger designs. For the latter one, only Jamialahmadi and Müller-Steinhagen (1992) and Kumar et al. (1976) related the mean bubble size to the initial bubble diameter. It should be noted that any radial distribution of the bubble size, $d_m(\xi)$, has been not yet reported since such data are hardly accessible with conventional techniques. However, $d_m(\xi)$ can be determined with ultrafast X-ray tomography as recently shown by Azizi et al. (2017).

2.2. Gas holdup

The effect of the superficial gas velocity on the gas holdup is commonly expressed as $\bar{\alpha}_g \propto U_g^n$ with $0.7 < n < 1.2$ for the homogeneous and $0.4 < n < 0.7$ for the heterogeneous flow regime (Basha et al., 2015, Shah et al., 1982, Reilly et al., 1986). In the heterogeneous flow regime, the contribution of small bubbles to the gas holdup is rather constant and equals the holdup at transition regime, whereas the large bubbles holdup continuously increases with increasing U_g (Kantarci et al., 2005, Krishna et al., 1991). In Table 3, the most common correlations for the prediction of the average gas holdup are summarized. All correlations to a greater or lesser extent consider the effects of liquid physical properties on the gas holdup. An increase in liquid viscosity reduces the gas holdup due to the formation of larger bubbles with higher rise velocity (Akita and Yoshida, 1973). Decreasing the surface tension results in smaller and more stable bubbles, which eventually lead to higher gas holdup and more uniform distribution of radial gas holdup (Kumar et al., 1976). Elevated gas density or higher operating pressure increase the gas holdup, which correlates inversely with the bubble size as mentioned above (Kantarci et al., 2005, Basha et al., 2015, Wilkinson and v. Dierendonck, 1990). The operating temperature mainly effects the liquid properties, which in turn influence the gas holdup (Basha et al., 2015). The available gas holdup correlations show some inconsistencies with regard to superficial gas velocity and physical properties. Kumar et al. (1976) and Reilly et al. (1986) considered gas and liquid phase densities and surface tension, while Hughmark (1967) considered the densities only. Kawase et al. (1992) and Hikita et al. (1980) considered liquid viscosity and density in their gas holdup correlations. The column diameter is considered by Akita and Yoshida (1973), Behkish et al. (2006), Sal et al. (2013), Krishna and Ellenberger (1996) and Nedeltchev and Schumpe (2008). The effect of the sparger design was emphasized in several studies (Luo et al., 1999, Akita and Yoshida, 1973). In particular, the introduction of small bubbles results in high gas holdups (Kantarci et al., 2005). The sparger design, however, is ignored in the correlations. Only Behkish et al. (2006) and Sal et al. (2013) considered the orifice size as a decisive parameter. By dividing the gas holdup into contributions of large and small bubbles, Krishna and Ellenberger (1996) developed a gas holdup correlation for the churn-turbulent regime, called the two-bubble class model. The shape of the bubbles was also considered in the development of the gas holdup correlations, e.g. Nedeltchev and Schumpe (2008) proposed a correlation assuming ellipsoidal bubbles.

Table 3: Most common correlations for the prediction of the gas holdup.

Reference	Correlation
Kumar et al. (1976)	$\bar{\alpha}_g = 0.728U' - 0.485U'^2 + 0.0975U'^3$ $U' = U_g \left(\frac{\rho_l^2}{\sigma(\rho_l - \rho_g)g} \right)^{0.25}$
Hughmark (1967)	$\bar{\alpha}_g = (2 + (\frac{0.35}{U_g})(\frac{\rho_l \rho_g}{72})^{1/3})^{-1}$
Reilly et al. (1986)	$\bar{\alpha}_g = 0.009 + 296U_g^{0.44} \rho_l^{-0.98} \sigma^{-0.16} \rho_g^{0.19}$
Kawase et al. (1992)	$\bar{\alpha}_g = \frac{0.0625(\frac{\rho_l U_g}{\mu_l})^{0.25}}{1 - 0.0625(\frac{\rho_l U_g}{\mu_l})^{0.25}}$
Hikita et al. (1980)	$\bar{\alpha}_g = 0.672f \left(\frac{U_g \mu_l}{\sigma} \right)^{0.578} \left(\frac{\mu_l^4 g}{\rho_l \sigma^3} \right)^{-0.131} \left(\frac{\rho_g}{\rho_l} \right)^{0.062} \left(\frac{\mu_g}{\mu_l} \right)^{0.107}$ <p>for pure liquids $f = 1$</p>
Akita and Yoshida (1973)	$\frac{\bar{\alpha}_g}{(1 - \bar{\alpha}_g)^4} = f \left(\frac{D^2 \rho_l g}{\sigma} \right)^{1/8} \left(\frac{g D^3 \rho_l^2}{\mu_l^2} \right)^{1/12} \left(\frac{U_g}{g \sqrt{D}} \right)$ <p>for pure liquids $f = 0.2$</p>
Behkish et al. (2006)	$\bar{\alpha}_g = 4.94 \times 10^{-3} \left(\frac{\rho_l^{0.415} \rho_g^{0.177}}{\mu_l^{0.174} \sigma^{0.27}} \right) U_g^{0.553} \left(\frac{p_T}{p_T - p_S} \right) \left(\frac{D}{D + 1} \right)^{-0.117} \Gamma^{0.053}$ $\Gamma = (K_d N d_o^\alpha)$ <p>K_d was reported at several points of ζ, where $\zeta = 100 N d_o^2 / D^2$</p>
Sal et al. (2013)	$\bar{\alpha}_g = 0.2278 \left(\frac{U_g^2}{d_o g} \right)^{0.7767} \left(\frac{d_o^3 \rho_l^2 g}{\mu_l^2} \right)^{0.3649} \left(\frac{d_o}{D} \right)^{0.4780} \left(\frac{d_o^2 \rho_l g}{\sigma} \right)^{0.3916} \left(\frac{D^4 U_g^2 \rho_l}{d_o^3 N^2 \sigma} \right)^{0.2402}$

Continued on next page...

Table 3 – continued from previous page.

Reference	Correlation
Krishna and Ellenberger (1996)	$\bar{\alpha}_g = \bar{\alpha}_{g,SB} + \bar{\alpha}_{g,LB}$ $\bar{\alpha}_{g,LB} = \frac{0.268}{D^{0.18}} \frac{(U_g - U_{df})^{4/5}}{(U_g - U_{df})^{0.22}}$ $\bar{\alpha}_{g,SB} = \bar{\alpha}_{gm,trans}$
Nedeltchev and Schumpe (2008)	$\bar{\alpha}_g = f \frac{2\bar{d}_e f_b S_B}{3\pi D^2 u_b}$ $\bar{d}_m = \bar{d}_e = (l^2 h)^{1/3}$ $l = \begin{cases} \frac{\bar{d}_e}{1.14 Ta^{-0.176}} & 2 < Ta < 6 \\ \frac{\bar{d}_e}{1.36 Ta^{-0.28}} & 6 < Ta < 16.5 \end{cases}$ $h = \begin{cases} 1.3 \bar{d}_e Ta^{-0.352} & 2 < Ta < 6 \\ 1.85 \bar{d}_e Ta^{-0.56} & 6 < Ta < 16.5 \end{cases}$ $Ta = \left(\frac{\rho_l u_b \bar{d}_e}{\mu_l} \right) \left(\frac{g \mu_l^4}{\rho_l \sigma^3} \right)^{0.23}$ $u_b = \sqrt{\frac{2\sigma}{\rho_l \bar{d}_e} + \frac{g \bar{d}_e}{2}}$ $S_B = \pi \frac{l^2}{2} \left(1 + \left(\frac{h}{l}\right)^2\right) \frac{1}{2e} \ln\left(\frac{1+e}{1-e}\right)$ $e = \sqrt{1 - \left(\frac{h}{l}\right)^2}$

125 In addition to the mean gas holdup correlations, the radial distribution of the gas holdup was also investigated in few studies (Walter and Blanch, 1983, Wu et al., 2001). A parabolic gas holdup distribution is known to evolve in the column cross-section accompanied by radial pressure gradients, which prompts liquid circulation pattern with rising liquid in the center and descending liquid near the wall. Apart from some experimental studies (Kumar et al.,

¹³⁰ 1997, Wu et al., 2008, Azizi et al., 2017), only few correlations for the radial gas holdup distribution, $\alpha_g(\xi)$, have been proposed as summarized in Table 4. These correlations are basically developed in terms of the dimensionless radius following a power law, where n defines the steepness of the holdup distribution. Ueyama and Miyauchi (1979) considered $n \approx 2$ for their experimental data and $\tilde{\alpha}_g$ as the radial chordal average gas holdup. Wu et al.
¹³⁵ (2001) included an additional parameter c , which determines the gas holdup value near the wall.

Table 4: Correlations for the prediction of the radial gas holdup profile.

Reference	Correlation
Ueyama and Miyauchi (1979)	$\alpha_g(\xi) = \tilde{\alpha}_g \left(\frac{n+2}{n} \right) (1 - \xi^n)$ <p>where $n \approx 2$</p>
Wu et al. (2001)	$\alpha_g(\xi) = \bar{\alpha}_g \left(\frac{n+2}{n+2-2c} \right) (1 - c\xi^n)$ $n = 2.188 \times 10^3 \left(\frac{DU_g(\rho_l - \rho_g)}{\mu_l} \right)^{-0.598} \left(\frac{U_g^2}{gD} \right)^{0.146} \left(\frac{g\mu_l^4}{(\rho_l - \rho_g)\sigma^3} \right)$ $c = 4.32 \times 10^{-2} \left(\frac{DU_g(\rho_l - \rho_g)}{\mu_l} \right)^{0.2492}$

2.3. Liquid velocity

The degree of liquid mixing is determined by the mean liquid circulation velocity, $U_{l,circ}$, which strongly effects conversion and selectivity of chemical reactions in bubble columns
¹⁴⁰ (Shimada et al., 2012). $U_{l,circ}$ is equal to the average ascending and descending liquid velocity of the mean liquid velocity distribution, $U_l(\xi)$. Due to limited information on $U_l(\xi)$, $U_{l,circ}$ is commonly estimated as proportional to $(DU_g)^m$ (Nottenkämper et al., 1983, Zehner, 1982, Degaleesan, 1997). In Table 5, correlations for $U_l(\xi)$ are given. These correlations are based on the centerline maximum velocity, $U_{l,max}$, whose correlations are also provided in this
¹⁴⁵ table. For $U_l(\xi)$, Walter and Blanch (1983) proposed a second order polynomial correlation considering the flow inversion point, which has been assigned to $\xi_{inv} = 0.7$. In their power law correlation, they applied the same coefficients for n and c as proposed for their gas holdup correlation.

2.4. Correlation derivation from complementary experimental data

The correlations compiled in Tables 1 to 5 allow initial estimations of the hydrodynamic parameters in bubble columns. These correlations are useful when only limited experimental data are available. However, it should be noted that the application ranges of the correlations in terms of flow regimes, physical properties, dimensions of bubble column and sparger design

Table 5: Correlations for the prediction of the radial and centerline liquid velocity profile.

Reference	Correlation
Walter and Blanch (1983)	$U_l(\xi) = U_{l,max}(1 - (\frac{\xi}{\xi_{inv}})^2)$ where $\xi_{inv} = 0.7$
Wu and Al-Dahhan (2001)	$U_l(\xi) = U_{l,max}(1 - 2.65n^{0.44}c\xi^{2.65n^{0.44}c})$
Zehner (1982)	$U_{l,max} = 0.737(U_g D)^{1/3}$
Riquarts (1981)	$U_{l,max} = (0.21gD)^{1/2}(\frac{U_g^3 \rho_l}{g\mu_l})^{1/8}$

155 are not explicitly mentioned for most of the correlations or are not consistent with each other.
 In the engineering and design concepts, usually a combination of correlations of the following
 hydrodynamic parameters, \bar{d}_i , \bar{d}_m , $d_m(\xi)$, $\bar{\alpha}_g$, $\alpha_g(\xi)$, $U_l(\xi)$, $U_{l,circ}$, respectively, are applied in
 the calculations. Dudley (1995) showed that \bar{d}_m and $\bar{\alpha}_g$ are needed from other correlations
 (Tables 2 and 4) to correlate the mass transfer. The interdependencies between \bar{d}_m and $\bar{\alpha}_g$
 160 correlations are unknown due to the incomparable experiments and procedures for the devel-
 opment of these correlations. Applying these correlations may result into strong deviations
 from the actual values. Thus, to improve the results, compatible correlations containing the
 interdependencies of hydrodynamic properties are needed. This can be achieved using an
 experiment, which all hydrodynamic properties are measured for the derivation of a set of
 165 "coupled" hydrodynamic correlations.

In our recent work, the potential of non-invasive measurement techniques, namely Ultra-
 fast X-ray Computed Tomography (UXCT) and Radioactive Particle Tracking (RPT), has
 been exemplarily illustrated for an advanced hydrodynamic analysis of bubble columns (Azizi
 170 et al., 2017). These complementary techniques enable access to the dynamics of both fluid
 phases. The data sets of these measurement techniques provide a unique basis for the devel-
 opment of hydrodynamic correlations. Hence, the detailed objective of this work is to derive
 hydrodynamic correlations for \bar{d}_i , \bar{d}_m , $d_m(\xi)$, $\bar{\alpha}_g$, $\alpha_g(\xi)$, $U_l(\xi)$ and $U_{l,circ}$ on the basis of experi-
 mental data from UXCT and RPT. These techniques are applied to measure gas and liquid hy-
 175 drodynamic properties at same operating conditions, column dimensions and sparger configu-
 rations.

Figure 1 highlights the chronological order in which the set of coupled hydrodynamic
 correlations are derived. (0 → 1) The inlet bubble diameter, \bar{d}_i is correlated from a single ori-
 fice/needle with using the Re_{d_o} and $Eöd_o$ based on the orifice diameter, d_o . (2) Subsequently,
 180 \bar{d}_i in terms of $Re_{\bar{d}_i}$ along with the sparger configuration $D(N \cdot \delta_p)^{-1}$ and gas/liquid properties

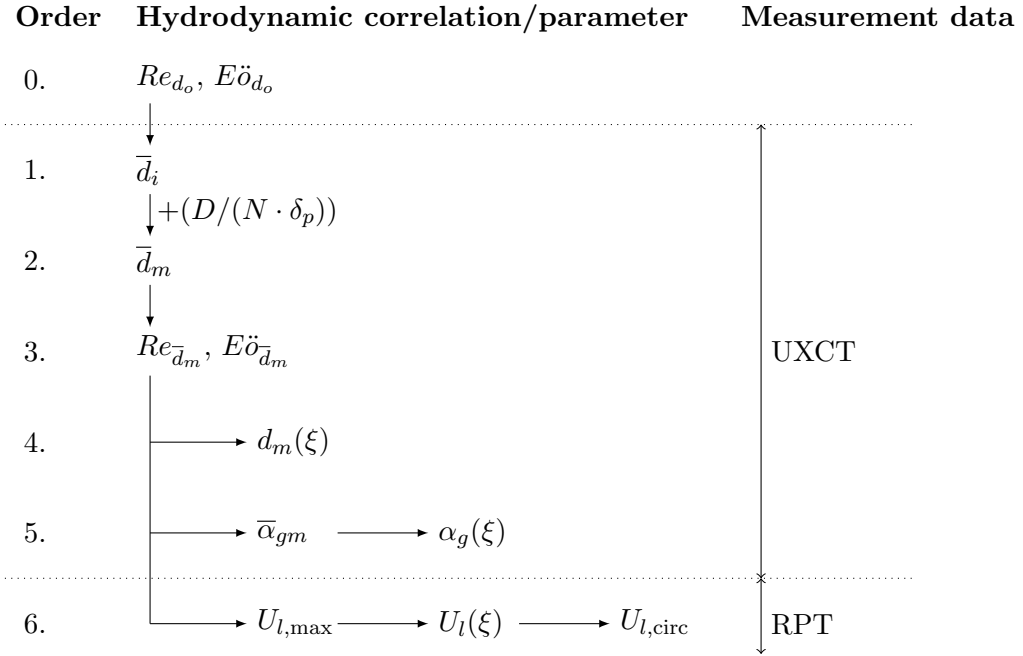


Figure 1: Procedure for the derivation of the set of coupled hydrodynamic correlations.

are employed to correlate the mean bubble diameter \bar{d}_m . $D/N\delta_p$ shows the ratio of bubble column diameter to the pitch size, D/δ_p divided by number of needles/orifices, N . With knowing this ratio, the pattern of installed needles/orifices are identical in our experiments.
 185 The lowest value of $D/N\delta_p$ shows the compact installation of needles in the sparger. (3) \bar{d}_m is used as the characteristic length in $Re_{\bar{d}_m}$ and $Eö_{\bar{d}_m}$. (4 and 5) Hence, $D(N \cdot \delta_p)^{-1}$, $d_m(\xi)$, $\bar{\alpha}_g$ and the corresponding $\alpha_g(\xi)$ can be derived with using these dimensionless numbers and the
 190 sparger configuration. Up to now, for all the derived correlations UXCT experimental data is used. (6) To derive the $U_l(\xi)$ and $U_{l,circ}$ correlations, RPT experimental data are required.
 195 Steps 4, 5 and 6 are interchangeable, but are ordered here in a logical manner.

3. Experimental setup

The advanced measurement techniques UXCT and RPT were applied to a lab-scale bubble column. The experiments were performed at Indian Institute of Technology Delhi (IITD, India) and at Helmholtz-Zentrum Dresden-Rossendorf (HZDR, Germany) using RPT and
 195 UXCT, respectively. In order to ensure identical experimental conditions at either end, sparger and peripheral equipment were shipped to the respective labs and properties of the liquid phase were precisely matched.

3.1. Bubble column geometry and operating conditions

A cylindrical bubble column with an inner diameter of $D = 0.1$ m and a height of
 200 $H = 1.0$ m was used. Deionized water and air were used as liquid and gas phases, respectively, and the following liquid phase properties were determined: $\sigma = 70 \times 10^{-3}$ N/m, $\rho_l = 997$ kg/m³, $\mu_l = 0.001$ kg·m/s. The unaerated liquid height was adjusted at $H_0 = 0.70$ m. The bottom of the column was equipped with a needle sparger, which consists of three radially

separated gas plenum sections with a height of $H_p = 0.20$ m. Different numbers of needles with various sizes can be installed via 115 connection points similar to Luer-Lock connections.
205 The Luer lock connection bases of needles are implemented inside the sparger. The full metal section of needles is in contact with liquid. The inserted length of needles is 30 mm for all of the needles in different sparger configurations. In Table 6, the applied sparger configurations A to F are shown with corresponding specifications. The radially separated plenum sections
210 are indicated with dotted red line.

Table 6: Sparger configurations with number of needles, N pitch size, δ_p and the dimensionless number $\frac{D}{N\delta_p}$.

	A	B	C	D	E	F
N	13	19	31	42	73	115
δ_p (mm)	27	21	16	14	9	8
$\frac{D}{N\delta_p}$	0.28	0.25	0.20	0.17	0.15	0.10

The superficial gas velocity was adjusted via three mass flow controllers (OMEGA, 2xFMA-2608A, 1xFMA-2609A) at $U_g = 1.0, 3.2, 5.3$ and 9.5 cm/s, respectively, while each gas plenum section of the sparger was separately connected to a mass flow controller. The gas flow rate through every section was adjusted according to the respective number of installed needles.
215 Needles of 30 mm length with different inner diameters were installed. Table 7 summarizes the experimental matrix with the corresponding sparger configurations. The experimental matrix was chosen to cover both the homogeneous and heterogeneous flow regime via various superficial gas velocities while the inlet bubble size has been controlled by needle size and number installed in sparger.

220 3.2. Ultrafast X-ray Computed Tomography (UXCT)

Figure 2 shows the bubble column with the installed UXCT setup. Basically, UXCT produces cross-sectional images of the transient two-phase flows (reconstructed images with 240 pixels per 120 mm) at a scanning rate of 1000 frames per second (fps). An electron beam is focused on a tungsten target generating an X-ray spot. The electron beam is swept
225 periodically along the target surrounding the bubble column so that the produced X-ray fan penetrates the column from different angles. The arriving X-ray intensity is recorded with a detector ring, which consists of multiple detector elements co-aligned with the target. Each revolution of the electron beam around the bubble column provides X-ray intensity data for the reconstruction of one cross-sectional image at time step t (Fischer and Hampel, 2010,
230 Bieberle et al., 2011). For the individual post-processing steps and the accuracy analysis of UXCT measurements, the reader is referred to Azizi et al. (2017). The experiments to determine bubble size and gas holdup were conducted at heights of $H_{\text{meas}} = 0.01, 0.1, 0.3$ and 0.5 m above the needles head of sparger. At each height, the mean values as well as the radial profiles of bubble size and gas holdup were calculated via averaging over the whole cross-section and circumferentially, respectively. According to Fischer et al. (2008), a frame rates
235

Table 7: Experimental matrix.

Experiment No.	U_g (cm/s)	d_o (mm)	N (-)	Sparger type
1	1.0	0.22	115	F
2	3.2	0.22	115	F
3	5.3	0.22	115	F
4	9.5	0.22	115	F
5	1.0	0.57	19	B
6	3.2	0.57	31	C
7	5.3	0.57	42	D
8	9.5	0.57	73	E
9	1.0	0.95	13	A
10	3.2	0.95	19	B
11	5.3	0.95	31	C
12	9.5	0.95	42	D

of at least 1000 fps are required to produce sharp phase distribution images with a spatial resolution of about 1 mm. In this work, the minimum detected bubble diameter is 1 mm. The experimental data at $H_{\text{meas}} = 0.01$ m are used to determine the initial bubble size at the sparger, due to capability of releasing the bubbles without breakup and coalescence at the top of the needles. The applied dynamic high-speed imaging in UXCT experiments is not prone to typical dynamic bias errors known from time-averaging probe measurement techniques (Fischer et al., 2008). The measurement time for each experiment was 10 s. Considering the hardware limitation and the costs of measurements, the longer measurement times were not possible. However, the identified bubbles are around few thousand in UXCT measurements, which provides statistically reliable data in 10 s.

3.3. Radioactive Particle Tracking (RPT)

Figure 3 shows the bubble column with the RPT setup using eight detectors located at four different axial heights. In the RPT experiments, the tracer particle is a radioactive isotope (Sc_{46}) with a half-time of 83 days, which decays by beta emission followed by gamma-ray emission. The radioactive particle is encapsulated in a sphere of polymeric material with 2 mm diameter. The whole tracer particle has an equivalent density similar to the liquid phase to ensure that it is neutrally buoyant and follows the liquid flow precisely (Azizi et al., 2017). Stokes number, St characterizes the motion of particles in a continuous fluid. In fact, $St < 1$ is essential to guarantee following of the tracer particle closely to the liquid streamlines. In this work, the corresponding Stokes numbers of experiments are $0.04 < St < 0.15$. During the RPT measurements, the moving tracer particle continuously emits gamma photons. The bubble column is surrounded by an optimized arrangement of scintillation detectors (Roy et al., 2002). The incident photons hit the NaI crystals in the detectors and scintillate into visible light. The visible light passes through the photomultiplier and gets converted into electrical pulses. The RPT measurement frequency is 50 Hz. The counted pulses of the detectors for each time step decrease exponentially with increasing distance between

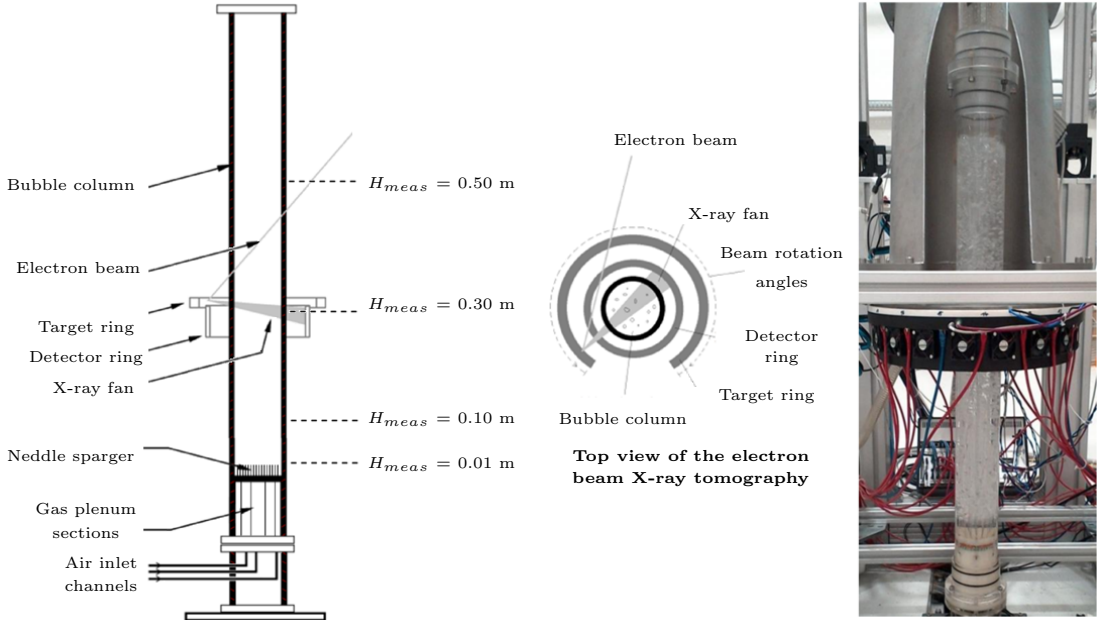


Figure 2: Sketch of the ultrafast X-ray tomography (UXCT) with the bubble column installation.

scintillation detector and tracer. Prior to the measurements, calibration data were recorded at multiple known positions of the tracer particle. At every individual measurement time step, the comparison of the photon counts of the detectors between measurement and calibration 265 data discloses the position of the tracer particle (Upadhyay et al., 2013). Eventually, the velocimetry data for the liquid phase can be obtained from RPT measurements based on known tracer positions at each time step of the measurement (Degaleesan et al., 2001). The measurement time for each experiment was approximately 20 hours to collect sufficient data for the reconstruction of the velocity field.

270 4. Results and discussion

4.1. Complementary experimental database

In this section, an overview of the gas phase flow morphology and the particle trajectories is provided, which is obtained via UXCT and RPT, respectively. Figure 4a illustrates the effect 275 of the sparger configuration on the liquid dispersion (particle trajectories) and gas structure (vertical coordinate represents the measurement time) via 3D stacked sequences of 1000 UXCT images obtained at $H_{\text{meas}} = 50$ cm during one second measurement time. The sparger configuration F consists of a large number of small needles, which accordingly produce small bubbles uniformly dispersed in the whole cross-section of the bubble column. With bigger needle size and lower number of installed needles (sparger structures B and A), the size of the bubbles 280 increases and larger bubbles accumulate in the center region of the column cross-section. Bubble size and the extent of distribution uniformity influence the liquid flow within the bubble column, which is shown in terms of particle trajectories from the RPT measurements in Figure 4b. Actual data acquisition in RPT is over several hours spanning thousands of trajectories. Here, the particle trajectories are visualized for a limited duration of 120 seconds showing 6000

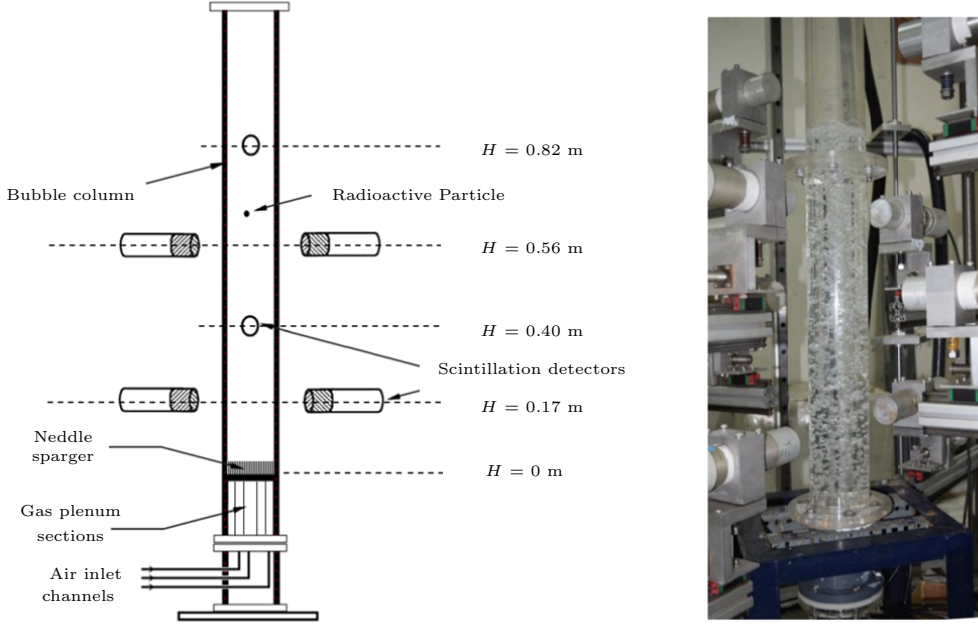
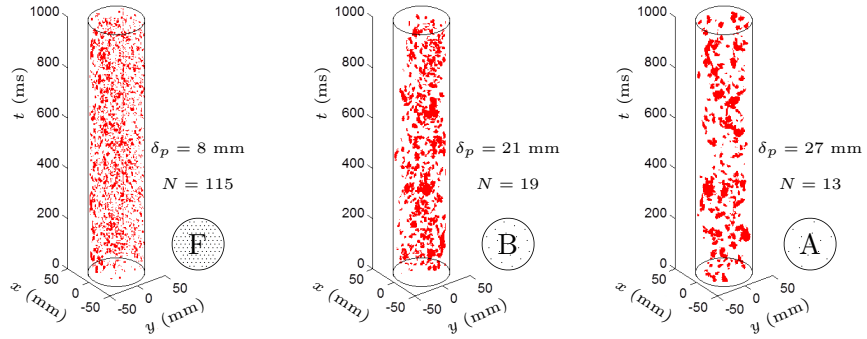


Figure 3: Sketch of the radioactive particle tracking (RPT) with installed detectors positioned around the bubble column.

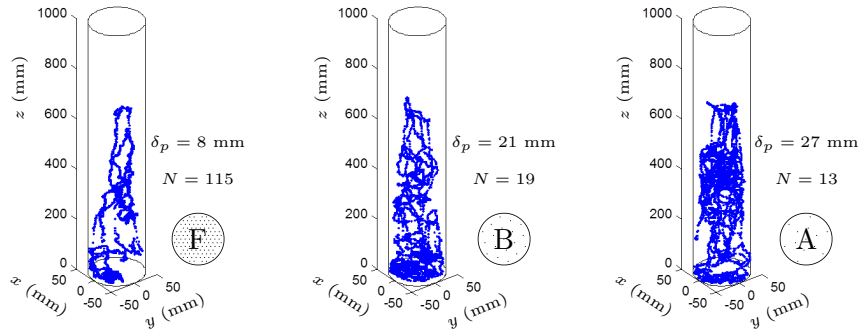
285 subsequent locations. The length and the dynamics of the trajectory (tracer particle path lines) indicate the liquid displacement, which is comparably low in the bubble column with the sparger structure F. This is due to small and uniform bubbles distributed evenly in the cross-section. Accordingly, the liquid mixing within the bubble column is low. The gas dynamics is increased due to larger bubbles released from the coarser sparger configurations B and A. As
290 a consequence, the drag force increases causing higher liquid velocities in the bubble column.

The effect of the superficial gas velocity on the gas phase structure is shown in Figure 5a at $H_{\text{meas}} = 50$ cm for the sparger structure F, which releases small bubbles of narrow size distribution. Gas holdup and bubble size increase with increasing superficial gas velocity
295 from 1.0 to 9.5 cm/s, accompanied by a decreasing uniformity of the gas holdup distribution. In Figure 5b the corresponding particle trajectories from 6000 subsequent particle locations (i.e. 120 seconds) show increasing displacement and dynamics at higher superficial gas velocities. The tracer trajectory at $U_g = 1.0$ cm/s consists mainly of longer rising and descending paths, while at larger superficial gas velocity, the tracer moves in a more random manner.
300 Gas bubble dispersions and particle trajectories at $U_g = 1.0$ cm/s belong to the homogeneous regime, while the increased fluctuations, the spiraling path of the bubbles as well as the intensified displacement of the tracer particle indicate transition ($U_g = 3.2, 5.3$ cm/s) and heterogeneous regimes ($U_g = 9.5$ cm/s).

305 In the following sections, the correlations for mean bubble size, gas holdup and liquid velocity are derived from UXCT and RPT experiments and compared with existing correlations. Experimental data from the literature, which are not used in developing of new correlations, were also applied to validate the developed correlations. The domain of definition of devel-



(a) 3D stacked sequences of 1000 binarized UXCT images during 1 s measurement at $H_{\text{meas}} = 50 \text{ cm}$.



(b) Tracer particle trajectory for 120 s measurement obtained via RPT.

Figure 4: Effect of different sparger structures at $U_g = 1.0 \text{ cm/s}$.

oped correlations are given in form of dimensionless numbers. Considering these domains,
 310 limited experimental data exist for the evaluation of the correlations. Thus, the proposed
 evaluation data consist of bubble columns with needle sparger and perforated plate. In the
 developed correlations, the sparger effect were considered in form of sparger configuration and
 initial bubbles diameter. The evaluation of developed correlations shows a fair agreement of
 experimental data at the low superficial gas velocities in the bubble columns with perforated
 315 plate sparger. To derive each of the radial distribution correlations for bubble size, gas holdup
 and liquid velocity, an optimization problem was solved to minimize the error of predicted
 radial property compared with the experimental data.

4.2. Bubble size correlations

Since the sparger generally effects the mean bubble size and liquid motion, the initial
 320 bubble size is correlated with the internal needle diameter considering also the operating
 conditions. Subsequently, the initial bubble size is applied as a characteristic length to correlate
 the mean bubble size in the column.

4.2.1. Initial bubble size at the sparger

The effective forces on determining bubble formation, expansion and detachment are in-
 325 $\rho_g \ll \rho_l$ (Geary and Rice, 1991,

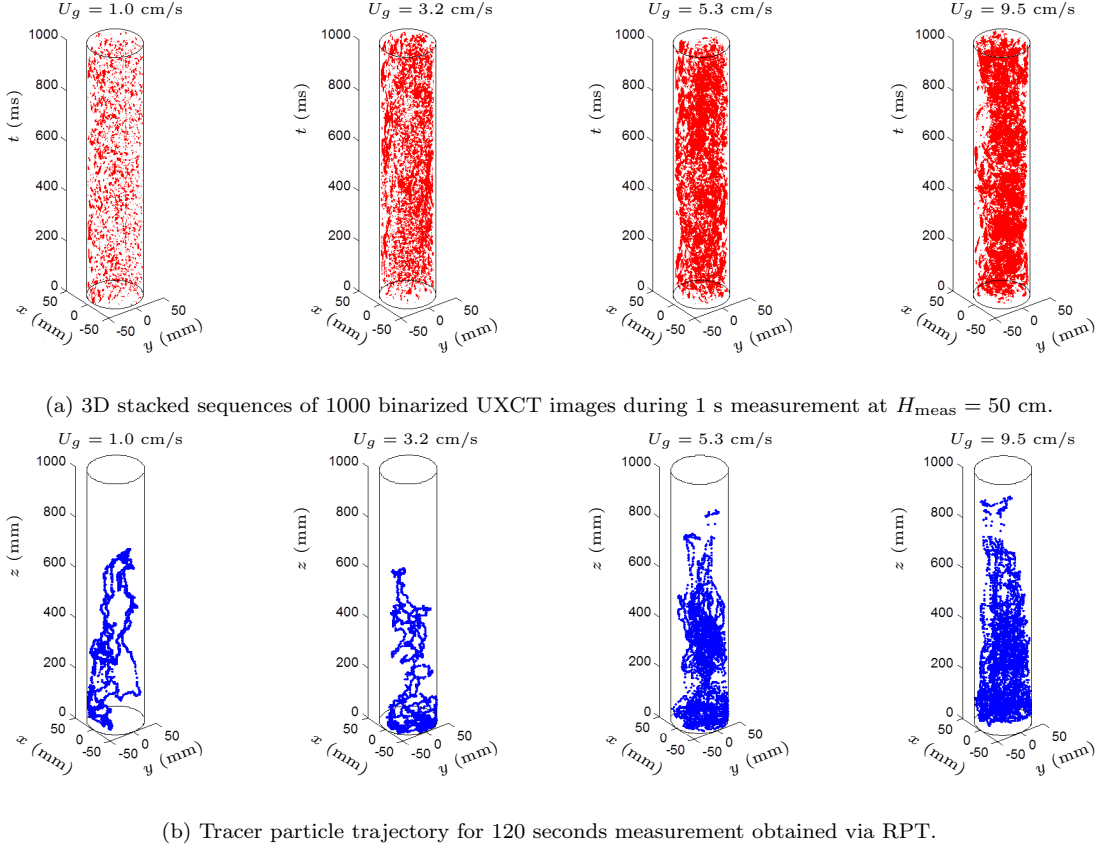


Figure 5: Effect of the superficial gas velocity in a bubble column with sparger configuration F ($\delta_p = 8$ mm, $N = 115$).

Tsuge and Hibino, 1978). Here, the orifice diameter d_o is used to calculate Re_{d_o} and $E\ddot{o}_{d_o}$ as

$$Re_{d_o} = \frac{\rho_l U_{go} d_o}{\mu_l} = \frac{\rho_l U g D^2}{\mu_l N d_o} \quad (1)$$

and

$$E\ddot{o}_{d_o} = \frac{\rho_l g d_o^2}{\sigma}. \quad (2)$$

According to dimensional analysis and Buckingham II theorem (see Appendix A), the equation for the initial bubble size can be written as $\bar{d}_i = b_1 d_o Re_{d_o}^{b_2} E\ddot{o}_{d_o}^{b_3}$. The unknown coefficients b_1 , b_2 and b_3 are calculated via nonlinear regression using the experimental data. The initial bubble size is derived as

$$\bar{d}_i = 2.19 \times 10^{-9} d_o Re_{d_o}^{1.46} E\ddot{o}_{d_o}^{-0.52}, \quad (3)$$

which is valid for $7 \times 10^{-3} < E\ddot{o}_{d_o} < 13 \times 10^{-2}$ and $4000 < Re_{d_o} < 40000$. In Figure 6, the prediction from the developed correlation is compared with the UXCT data. As shown, Equation 3 provides less than 20 % deviation, while the predictions of the correlations summarized in Table 2 are scattered in a wider range. Amongst the literature correlations, the model based on a force balance proposed by Geary and Rice (1991) shows the least deviations due to considering similar forces used to derive Equation 3.

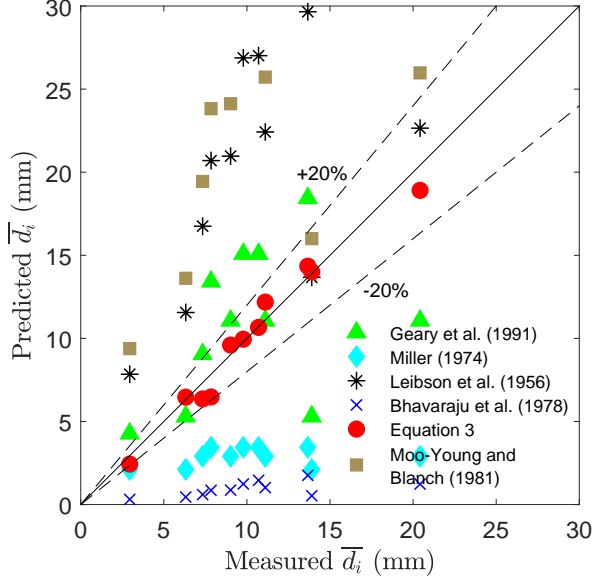


Figure 6: Parity plot of predicted and experimental initial (inlet) bubble diameters.

4.2.2. Mean bubble size

Previous correlations for the mean bubble size consider only the Reynolds number (see Table 2). However, the UXCT data reveal that the sparger configurations are decisive for the mean bubble size. Thus, the new correlation

$$\bar{d}_m = 6.75 \times 10^{-6} \frac{\sigma^2}{g\mu_l^2} \left(\frac{D}{N\delta_p} \right)^{0.47} Re_{\bar{d}_i}^{0.34} \quad (4)$$

with

$$Re_{\bar{d}_i} = \frac{\rho_l U_g \bar{d}_i}{\mu_l} \quad (5)$$

is proposed, which is valid for $0.1 < D/N\delta_p < 0.29$ and $20 < Re_{\bar{d}_i} < 3200$. As shown in the parity plot in Figure 7, the predictions from the previous correlations (see Table 2) deviate strongly from UXCT experiments. Increasing $Re_{\bar{d}_i}$ indicates increasing turbulence at the sparger region. The magnitude of \bar{d}_m depends on the net effect of turbulence-induced breakup and coalescence (Liao and Lucas, 2009, 2010). However, $Re_{\bar{d}_i}$ increases with increasing \bar{d}_i , which indicates an increase of the bubble-induced turbulence for the large bubbles. With increasing $Re_{\bar{d}_i}$ the mean bubble diameter increases by $Re_{\bar{d}_i}^{0.34}$. Furthermore, in Equation 4, the mean bubble diameter increases with decreasing pitch size of the sparger and increasing number of installed needles, resulting from an increasing coalescence rate.

4.2.3. Radial distribution of the mean bubble size

The radial bubble size distribution is correlated with a power law function, which can indicate larger bubbles in the center and a gradual reduction of the bubble size towards the wall (Kantarci et al., 2005, Basha et al., 2015) according to

$$d_m(\xi) = d_{max}(1 - c_d \xi^{n_d}) \quad (6)$$

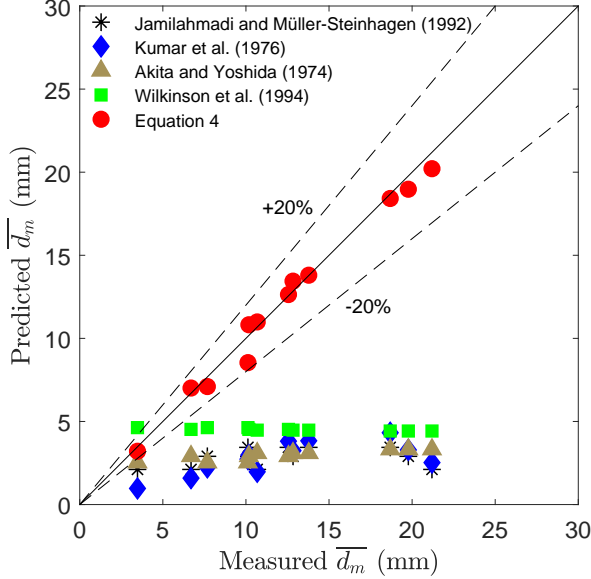


Figure 7: Parity plot of predicted and experimental mean bubble diameters.

with

$$d_{max} = \frac{\pi R^2 \bar{d}_m}{\int_0^1 2\pi R^2 \xi (1 - c_d \xi^{n_d}) d\xi} = \frac{(n_d + 2)\bar{d}_m}{(n_d + 2 - c_d)}. \quad (7)$$

Applying the dimensional analysis, the coefficients c_d and n_d depend mainly on Reynolds and Eötvös numbers based on the mean bubble diameter according to

$$c_d = 0.36 Re_{\bar{d}_m}^{0.14} E\ddot{o}_{\bar{d}_m}^{-0.06}, \quad (8)$$

$$n_d = 1.73 Re_{\bar{d}_m}^{1.42} E\ddot{o}_{\bar{d}_m}^{-2.83}, \quad (9)$$

360

$$Re_{\bar{d}_m} = \frac{\rho_l U_g \bar{d}_m}{\mu_l} \quad (10)$$

and

$$E\ddot{o}_{\bar{d}_m} = \frac{\rho_l g \bar{d}_m^2}{\sigma}, \quad (11)$$

where $56 < Re_{\bar{d}_m} < 2050$ and $4 < E\ddot{o}_{\bar{d}_m} < 66$ are the valid ranges. Figure 8 presents the UXCT experimental results for the radial bubble size distribution in comparison with the predictions of Equation 6 for different superficial gas velocity.

365 the radial bubble size distribution is rather flat, while a parabolic behavior is obtained with increasing superficial gas velocity. In Figure 8, applied sparger configurations and superficial gas velocities are F,B,E and C and 1.0, 3.2, 5.3 and 9.5 cm/s, respectively. Although different spargers and superficial gas velocities were applied, the developed correlation matches fairly well the radial bubble size distribution for all conditions. To the best of our knowledge, 370 correlations for the radial bubble size distribution in bubble columns are not available in the literature.

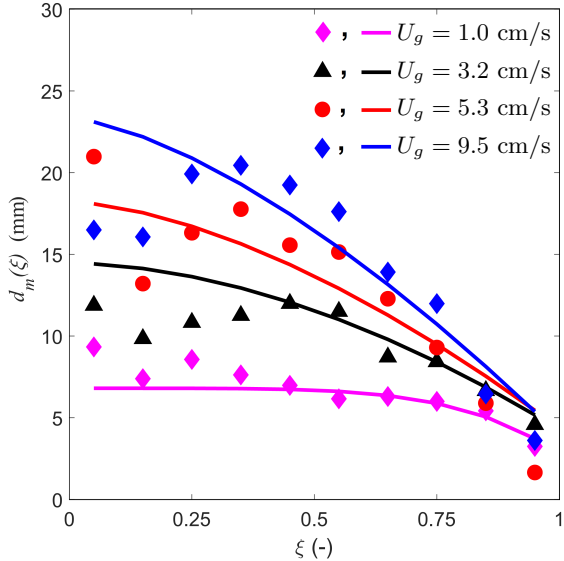


Figure 8: Comparison between experimental and predicted radial bubble size distributions (symbols indicate experimental data and lines the prediction according to Equation 6).

4.2.4. Comparison with experimental bubble size data from literature

Aiming for a bubble size correlation, which is valid beyond the own study, experimental data (Jamialahmadi and Müller-Steinhagen, 1992) and correlations from literature were compared with Equation 4 as shown in Figure 9. The experimental data of Jamialahmadi and Müller-Steinhagen (1992) are obtained for a bubble column of 10.5 cm diameter with a plate sparger with 1 mm orifice diameter distributed in a 18 mm triangular pitch ($N = 35$). The correlations of Akita and Yoshida (1973), Wilkinson et al. (1994), Kumar et al. (1976) show strong deviations. Equation 4 correctly accounts for the effect of the increasing superficial gas velocity considering the geometric features of the sparger. The developed correlation only slightly deviates from the experimental bubble size data, which might be due to the invasive nature of the probe measurements.

4.3. Gas holdup correlations

A similar approach for the development of the gas holdup correlation is applied. The total gas holdup correlation is developed based on $Re_{\bar{d}_m}$ and $E\ddot{o}_{\bar{d}_m}$ to account for the effect of \bar{d}_m and U_{go} . Similar to the radial bubble size distribution, a power law correlation is used to fit the radial gas holdup profile.

4.3.1. Total gas holdup

Considering $Re_{\bar{d}_m}$ and $E\ddot{o}_{\bar{d}_m}$ as defined in Equations 10 and 11, the total gas holdup is derived as

$$\bar{\alpha}_g = 1.1 \times 10^{-3} Re_{\bar{d}_m}^{1.12} E\ddot{o}_{\bar{d}_m}^{-0.89}. \quad (12)$$

The parity plot in Figure 10 compares results of correlations and experimental data using Equation 12 and the available total gas holdup correlations from the literature (see Table 3). It should be mentioned that most of the available correlations ignore the sparger design and thus, deviate strongly from the experimental results. Only the correlations of Behkish et al.

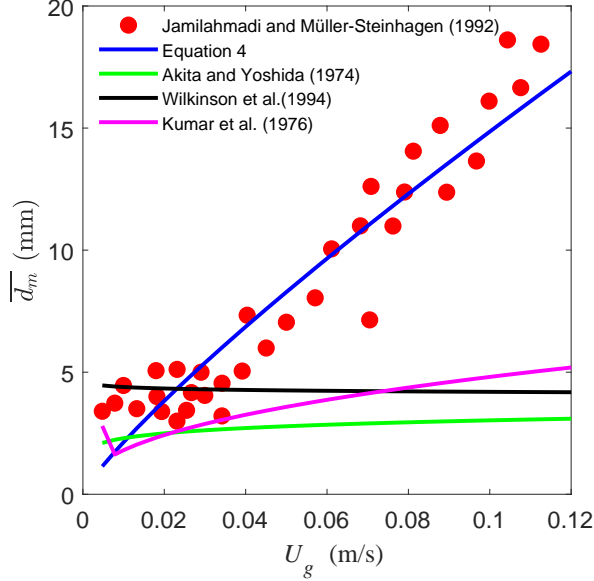


Figure 9: Prediction of the mean bubble diameter as a function of the superficial gas velocity.

395 (2006) and Sal et al. (2013) consider the sparger orifice diameter and the number of holes. The sparger configurations are considered well in the correlation of Behkish et al. (2006) with introducing the sparger parameter Γ , while Sal et al. (2013) applied N and d_o directly in the correlation. The effect of the bubble size on the gas holdup was not considered in their correlations. As mentioned in various studies, the total gas holdup increases with decreasing
400 bubble size (Deen et al., 2010). Equation 12 shows a good agreement between experimental and predicted total gas holdup.

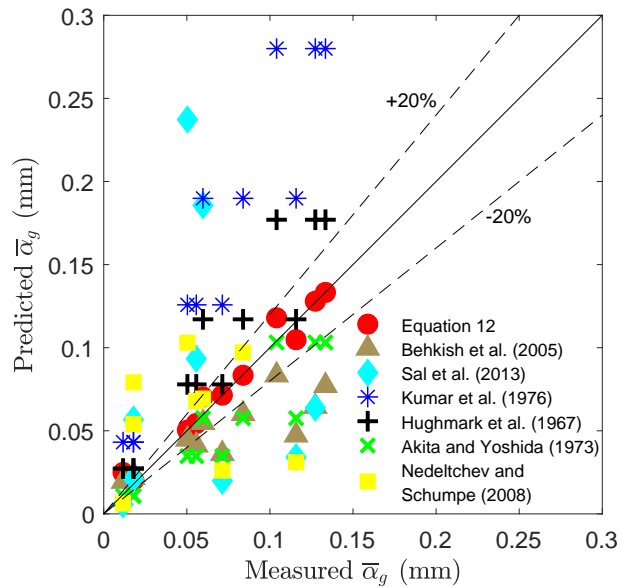


Figure 10: Parity plot of predicted and experimental total gas holdup data.

4.3.2. Radial gas holdup distribution

The developed correlation for the radial gas holdup distribution follows the approach of Wu et al. (2001) except for the coefficients, which are modified according to UXCT experimental results. The parameters of the correlation are correlated with $Re_{\bar{d}_m}$ and $E\ddot{o}_{\bar{d}_m}$ (Equations 15,16). In the correlation, the gas holdup in the center reduces gradually towards the column wall according to

$$\alpha_g(\xi) = \alpha_{g,max}(1 - c_\alpha \xi^{n_\alpha}). \quad (13)$$

The maximum gas holdup is defined as

$$\alpha_{g,max} = \frac{\pi R^2 \bar{\alpha}_g}{\int_0^1 2\pi R^2 \xi (1 - c_\alpha \xi^{n_\alpha}) d\xi} = \frac{(n_\alpha + 2) \bar{\alpha}_g}{(n_\alpha + 2 - c_\alpha)} \quad (14)$$

with

$$c_\alpha = 0.65 Re_{\bar{d}_m}^{-0.30} E\ddot{o}_{\bar{d}_m}^{0.68} \quad (15)$$

and

$$n_\alpha = 0.23 Re_{\bar{d}_m}^{0.39} E\ddot{o}_{\bar{d}_m}^{-0.18}. \quad (16)$$

Considering $Re_{\bar{d}_m}$ and $E\ddot{o}_{\bar{d}_m}$ (Equations 10 and 11), the coefficients c_α and n_α are chosen to properly predict the radial gas holdup profile, where $0.26 < c_\alpha < 0.93$ and $0.83 < n_\alpha < 2.16$ are the valid ranges. Figure 11 compares the UXCT measurement data with the predictions of Equation 13 using the coefficients of Wu et al. (2001) and the newly derived coefficients. The applied sparger configurations and superficial gas velocities in experiments and correlations are F,B,E and C and 1.0, 3.2, 5.3 and 9.5 cm/s, respectively. As shown in Table 4, the correlation of Wu et al. (2001) does not depend on the gas sparger and deviations increase with increasing superficial gas velocity. The developed correlation matches the radial gas holdup distribution fairly well. At low gas flow rate with small and uniform bubble size distribution, the radial gas holdup profile is rather flat, while the radial gas holdup distribution has a parabolic shape at high gas flow rates.

4.3.3. Comparison with experimental gas holdup data from literature

Figure 12a shows the behavior of the total gas holdup for increasing superficial gas velocity in a bubble column with an inner diameter of $D = 0.14$ m equipped with a perforated plate sparger with $N = 91$ orifices, whose diameter is $d_o = 0.4$ mm (Şal et al., 2013). The developed correlation shows fair agreements with the experimental gas holdup especially at the lower U_g . In Figure 12b, experimental data and predictions are shown for a bubble column with a needle sparger (Hooshyar et al., 2010). The diameter of the column is $D = 0.15$ m and the needle sparger consists of $N = 559$ needles with an inner diameter of $d_o = 0.8$ mm. The prediction with the new correlation fits the experimental data also well in comparison to the other correlations. However, it should be mentioned that the range of the dimensionless number presenting the sparger configuration does not match the suggested limits in Figure 12b, which causes the deviation in mean bubble diameter and total gas holdup. In both sub-figures of Figure 12, the linear increase and later nonlinear behavior of the experimental gas holdup shows the transition from homogeneous to heterogeneous

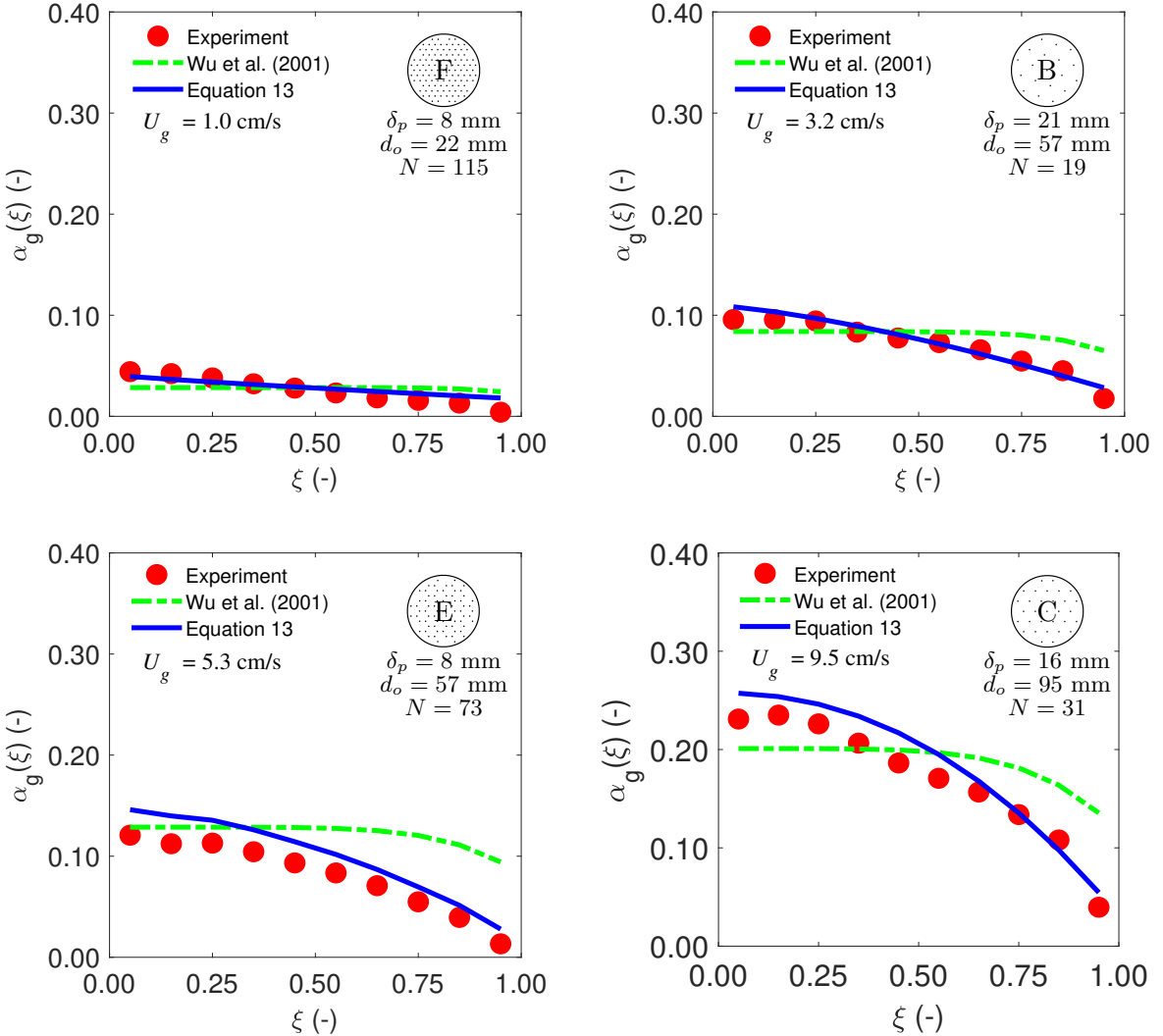


Figure 11: Comparison of the radial gas holdup profile using the correlation of Wu et al. (2001) and the own correlation vs. experimental data.

435 flow regime with increasing superficial velocity. However, the deviation of correlations is more pronounced at the transition points of the experimental data. The measurement and estimation of \bar{d}_m at higher U_g is difficult. Applying of the developed correlation based on \bar{d}_m , the bigger bubble size leads to lower gas holdups compared to the experiments. Due to the overestimation of \bar{d}_m , the gas holdup deviates from experimental data at higher U_g .

440

The radial gas holdup profile from the experimental study of Hooshyar et al. (2010) is plotted in Figure 13 together with the predictions using the developed correlation. (Equation 13) shows an excellent agreement, while the correlation of Wu et al. (2001) deviates from the experimental data.

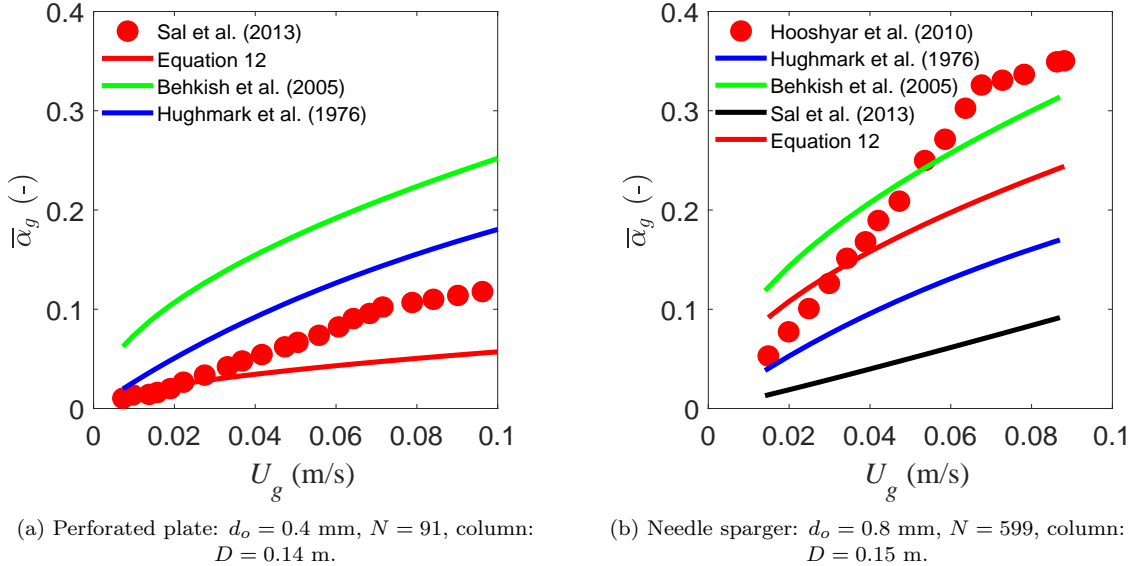


Figure 12: Total gas holdup in the bubble columns vs. superficial gas velocity.

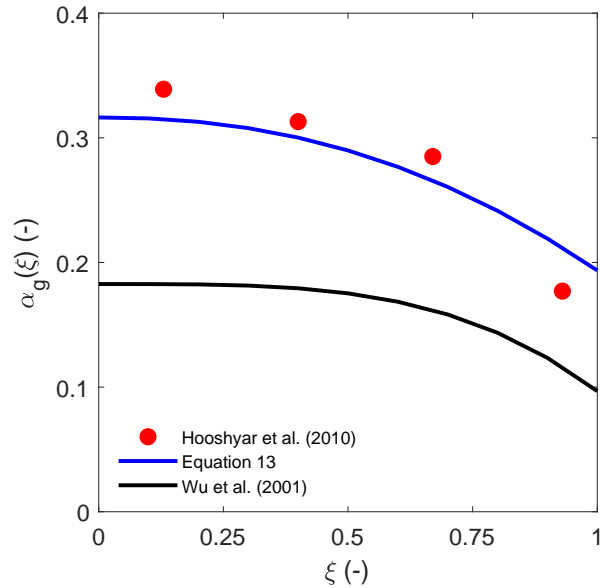


Figure 13: Radial gas holdup profile in a bubble column with a needle sparger ($D = 0.15$ m, $d_o = 0.8$ mm, $N = 599$, $U_g = 0.08$ m/s).

445 4.4. Liquid velocity correlations

The liquid velocity distributions were measured using the RPT technique. After reconstructing the RPT data, the liquid velocity field is obtained as cross-sectional view through the center of the bubble column (see Figure 14). The liquid velocity profile is well-developed at a height of approximately 20 cm above the sparger. To obtain the liquid circulation pattern within the bubble column, the axial liquid velocity is averaged over a range from 20 to 50 cm above the sparger to exclude sparger and free surface effects.
 450

The cross-sectional time averaged liquid velocity of the bubble column is zero, while the time-averaged liquid flow involves upward and downward flows in the axial direction. In the
 455 following sections, correlations are developed for the prediction of the radial distribution of the axial velocity and the mean circulation velocity of the liquid phase.

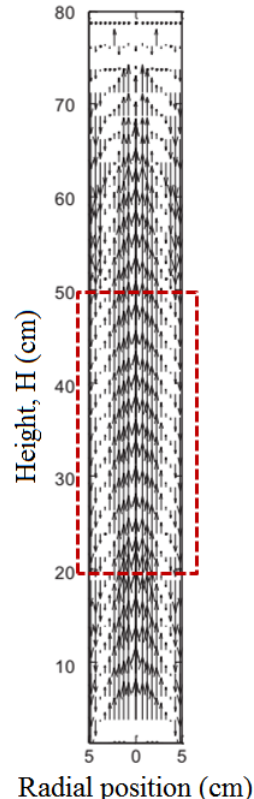


Figure 14: Averaging window along the height of bubble column for the liquid velocity.

4.4.1. Radial distribution of the liquid velocity

The velocity distribution involves a maximum in the center of the bubble column, which reduces gradually from the center to the inversion point. At the inversion point, the liquid
 460 velocity reaches zero and then, the liquid flow direction changes to downward flow between the inversion point and the wall. Theoretically, the liquid velocity follows the non-slip condition at the wall. However, the thickness of the boundary layer is very small and the experimental RPT data show the liquid velocity is not zero near to the wall. For this reason, a third order polynomial equation is considered for the liquid velocity distribution that accounts for the
 465 liquid flow behavior in the bubble column. However, the following boundary conditions are required as a set of constraints to establish the uniqueness of the flow field: maximum velocity at the ($\partial U_l / \partial \xi = 0$ and $U_l = U_{l,max}$ at $\xi = 0$), zero velocity at the inversion point ($U_l = 0$ at $\xi = \xi_{inv}$) and partial slip velocity at the wall ($\phi(\partial U_l / \partial \xi) + (1 - \phi)U_l = 0$ at $\xi = 1$). The parameter ϕ is the specularity coefficient, which varies between zero (smooth wall) and one

⁴⁷⁰ (rough wall). Here, $\phi = 0.25$ is considered. Applying these conditions results in

$$U_l(\xi) = a_0\xi^3 + a_1\xi^2 + a_2 \quad (17)$$

with

$$a_0 = a_2 \frac{(1 + \phi) - (1 - \phi)\xi_{inv}^2}{(1 + \phi)\xi_{inv}^3 - (1 + 2\phi)\xi_{inv}^2}, \quad (18)$$

$$a_1 = a_2 \frac{(1 + 2\phi) - (1 - \phi)\xi_{inv}^3}{(1 + \phi)\xi_{inv}^3 - (1 + 2\phi)\xi_{inv}^2} \quad (19)$$

and

$$a_2 = U_{l,max}. \quad (20)$$

The parameters $U_{l,max}$ and ξ_{inv} depend on the structure of the applied sparger, $Re_{\bar{d}_m}$ and $E\ddot{o}_{\bar{d}_m}$ (defined in Equations 10 and 11) according to

$$U_{l,max} = 0.02 \left(\frac{\sigma}{\rho_l \bar{d}_m} \right)^{0.50} \left(\frac{D}{N \delta_p} \right)^{-0.78} E\ddot{o}_{\bar{d}_m}^{0.87} \quad (21)$$

and

$$\xi_{inv} = 0.37 Re_{\bar{d}_m}^{0.05}. \quad (22)$$

Predicting the maximum liquid velocity with the available correlations in the literature (see Table 5) is not possible, because the effect of the sparger structure on the liquid velocity is neglected. In Figure 15, the assessment of the radial velocity distribution correlations is shown in comparison with the RPT experiments. Here, the applied configurations of the sparger and superficial gas velocities are F,B,E and C and 1.0, 3.2, 5.3 and 9.5 cm/s respectively. This way, the radial distributions of bubble size (Figure 8), gas holdup (Figure 11) and liquid velocity (Figure 15) can be compared at identical operating conditions. Contrary to Wu and Al-Dahhan (2001), the inversion point of the experimental data is below 0.7. The inversion point in the new developed correlation depends on $Re_{\bar{d}_m}$. Compared with the new correlation, one of Wu and Al-Dahhan (2001) deviates from the experimental results in predicting the radial liquid velocity.

4.4.2. Mean liquid circulation velocity

The mean liquid circulation velocity represents the degree of liquid mixing in the bubble column. The following correlation is based on sparger configuration and Reynolds number (defined in Equation 10) according to

$$U_{l,circ} = 0.79 U_{l,max} E\ddot{o}_{\bar{d}_m}^{-0.09}. \quad (23)$$

The mean liquid circulation velocity is the absolute average liquid velocity from the center to the inversion point (or from the inversion point to the wall). Considering the radial distributions of liquid velocity and gas holdup, the mean liquid velocity is derived as

$$U_{l,circ} = \frac{\int_0^{\xi_{inv}} U_l(1 - \alpha_g) R^2 \xi d\xi}{\int_0^{\xi_{inv}} (1 - \alpha_g) R^2 \xi d\xi}. \quad (24)$$

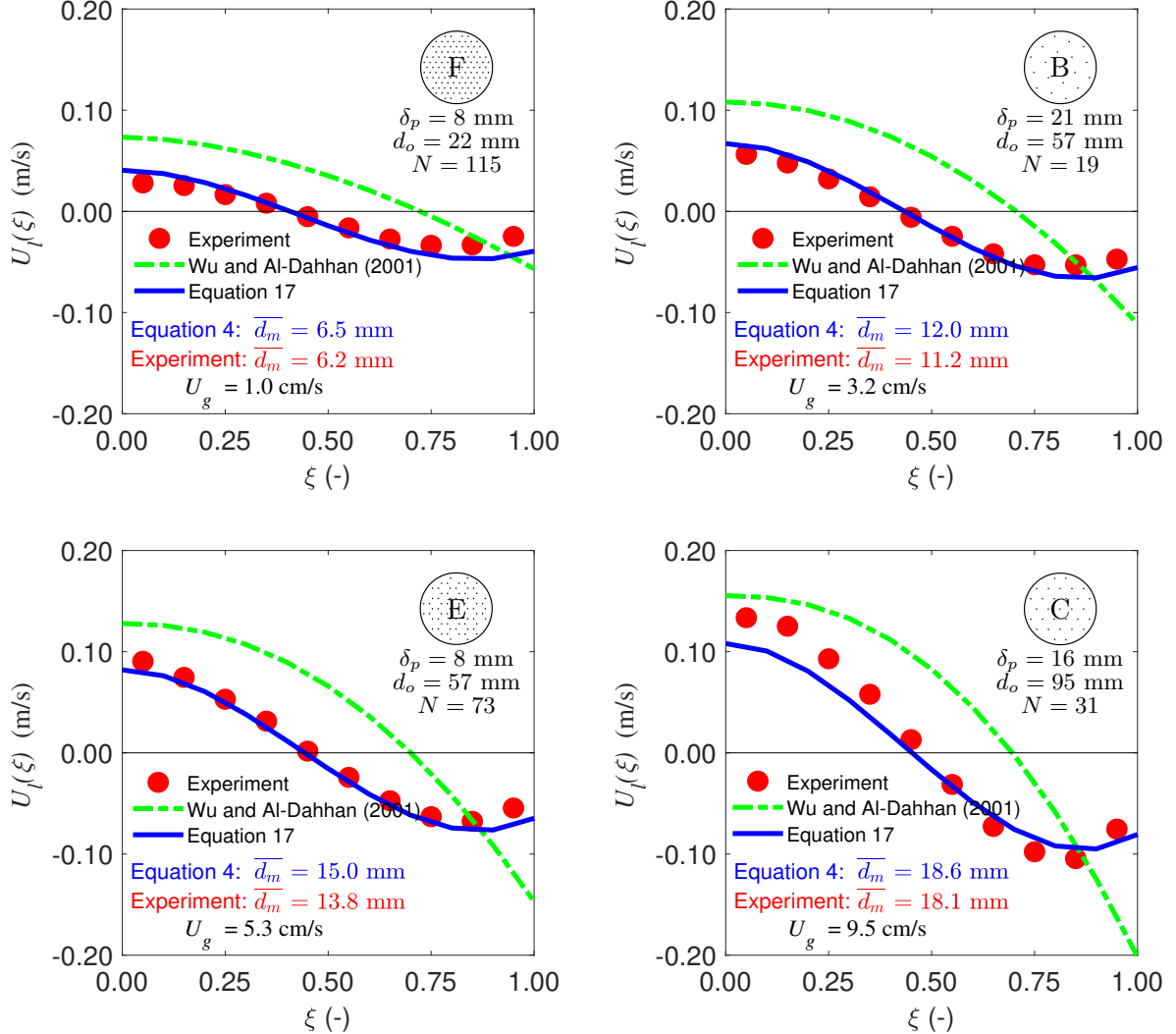


Figure 15: Comparison of the radial liquid velocity distribution by the correlation of Wu and Al-Dahhan (2001) and by the new correlation with the experimental data from RPT (this work).

The developed correlations for gas holdup and radial liquid distribution (Equations 13 and 17) can be applied in Equation 24 for calculating $U_{l,circ}$. As discussed in the introduction section, most researchers correlated $U_{l,circ}$ based on $(DU_g)^m$ (Nottenkämper et al., 1983, Zehner, 1982, Degaleesan, 1997). Nottenkämper et al. (1983) applied $m = 0.4$ based on their experiments. However, the prediction deviates from RPT experimental data at low U_g values (see Figure 16), while fair agreement is obtained for high U_g values. The developed correlation for the mean liquid circulation velocity predicts the experiments correctly considering the influence of the sparger configurations.

4.4.3. Comparison with experimental liquid velocity data from literature

In Figure 17, the predictions using the proposed radial liquid distribution correlation are compared with various experimental bubble column data from the literature. Degaleesan et al. (2001) applied a perforated plate sparger consisting of 61 orifices with an inner diameter of 0.4

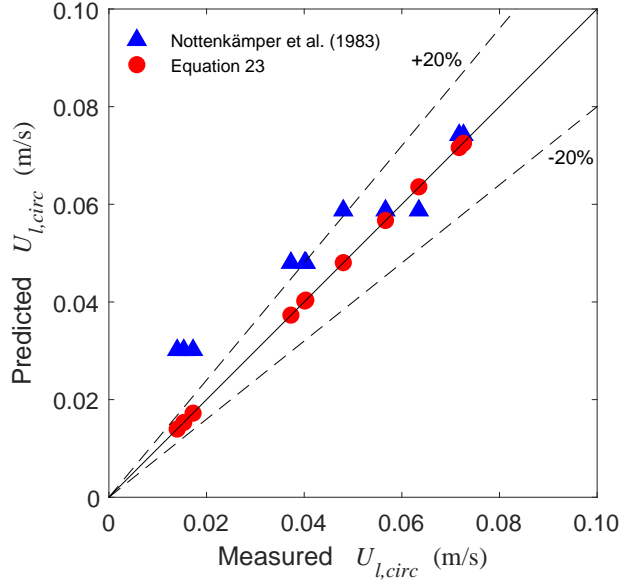


Figure 16: Parity plot of predicted and measured mean liquid circulation velocity.

mm and a pitch size of 15 mm for a column diameter of $D = 0.14$ m. The prediction especially near the wall is better to the correlation of Wu and Al-Dahhan (2001). The results of Wu and Al-Dahhan (2001) are based on the velocity predicted by the correlation of Riquarts (1981),
510 which shows a better agreement than the correlation of Zehner (1982) for the centerline velocity. The error of the developed correlation decreases with increasing superficial gas velocity.

Figure 18 presents experimental data from Sommerfeld and Bröder (2009) for a bubble
515 column diameter of $D = 0.14$ m operated with a needle sparger consisting of 50 needles with an inner diameter of 0.4 mm and a pitch size of 12 mm. The predicted velocity distribution for the needle sparger fairly agrees with the experimental data. The centerline velocity obtained from Wu and Al-Dahhan (2001) is estimated by applying the correlation of Riquarts (1981). Again, applying the centerline velocity of Riquarts (1981) gives a better estimation than the
520 correlation of Zehner (1982) for the centerline velocity.

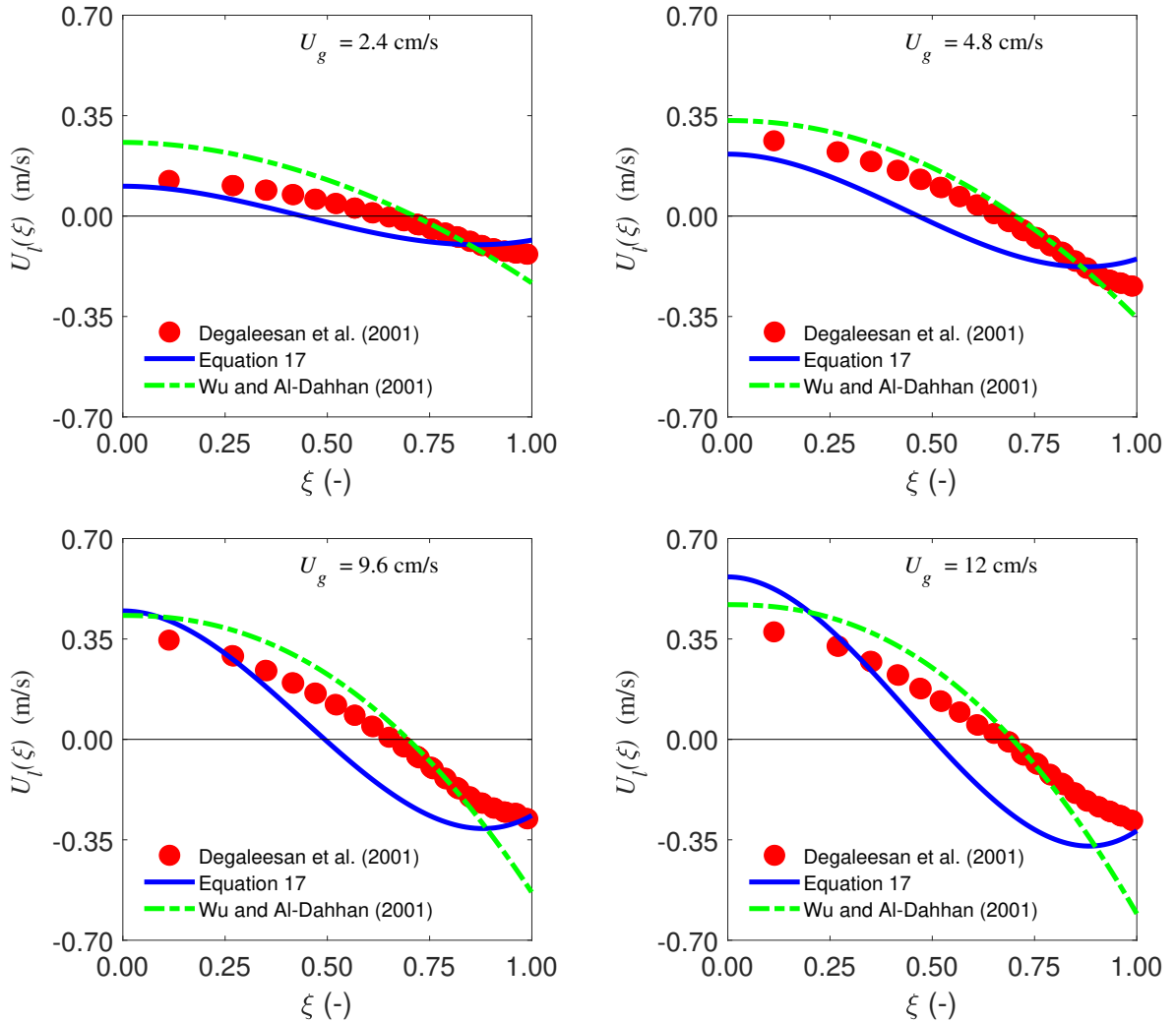


Figure 17: Liquid velocity distribution in a bubble column with a perforated plate.

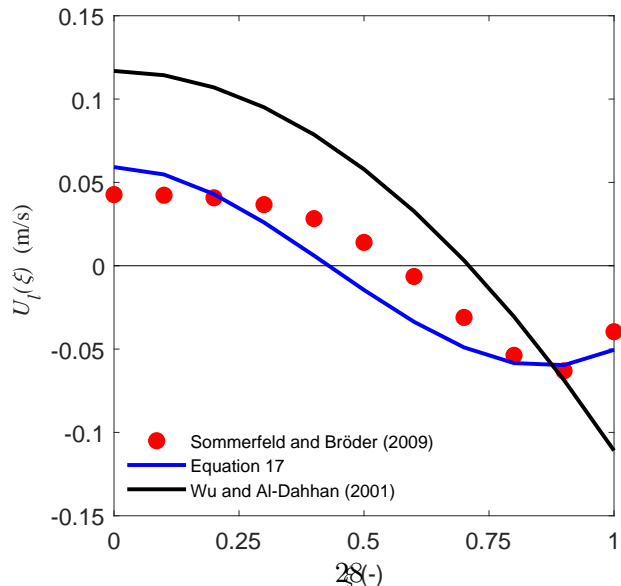


Figure 18: Liquid velocity distribution in a bubble column with a needle sparger ($U_g = 0.29 \text{ cm/s}$).

5. Conclusions

Hydrodynamic correlations are derived for bubble columns using complementary experimental data of UXCT and RPT measurements. UXCT is employed for gas phase dynamics, while RPT is used to obtain liquid phase dynamics. The measurements are performed for
525 a bubble column with identical geometrical dimensions and operating conditions as well as sparger configurations. The correlations are derived using the Buckingham Π theorem and a complete set of coupled hydrodynamic correlations for $\{\bar{d}_i, \bar{d}_m, d_m(\xi), \bar{\alpha}_g, \alpha_g(\xi), U_l(\xi), U_{l,circ}\}$ is given in the Equations (3, 4, 6, 12, 13, 17 and 23). These correlations are “one-way” coupled as illustrated in the derivation procedure. First, \bar{d}_i is correlated and is in turn
530 employed to derive the correlation for \bar{d}_m . Subsequently, characteristic dimensionless numbers regarding the complex hydrodynamics ($Re, Eö$) on basis of \bar{d}_m along with the sparger configuration $D/(N \cdot \delta_p)$ are used to derive correlations of $d_m(\xi), \bar{\alpha}_g$ (and corresponding $\alpha_g(\xi)$) and $U_l(\xi)$ (and corresponding $U_{l,circ}$). The validity range of the derived correlations are $0.1 < D/(N \cdot \delta_p) < 0.29$, $56 < Re_{\bar{d}_m} < 2050$ and $4 < Eö_{\bar{d}_m} < 66$. Eventually, the general
535 predictability of the developed correlations is also confirmed with experimental data from the literature obtained for different columns, sparger structures and operating conditions. As a future work, additional experiments for presenting dependency of developed correlations on physical properties are desired.

Acknowledgement

540 The authors gratefully acknowledge the financial support of the European Research Council (ERC Starting Grant, Grant Agreement No. 307360). Salar Azizi would like to thank the Indian Institute of Technology Delhi (IITD) and the technicians (Brahm Prakash Arya and Naresh Kumar) for the support during the visit at the Institute.

Nomenclature

Symbols

a_0	First coefficient of the polynomial radial liquid velocity correlation (Eq. 18), m/s
a_1	Second coefficient of the polynomial radial liquid velocity correlation (Eq. 18), m/s
a_2	Third coefficient of the polynomial radial liquid velocity correlation (Eq. 18), m/s
c	Parameter for radial gas holdup and liquid velocity distributions
c_d	Parameter for the radial bubble size distribution
c_α	Parameter for the radial gas holdup distribution
D	Bubble column diameter, m
\bar{d}_e	Characteristic Eddy length, m
\bar{d}_i	Initial bubble diameter at the gas sparger, m
\bar{d}_m	Mean bubble diameter in the bubble column, m
\bar{d}_{mL}	Mean large bubble diameter (Table 2), m
\bar{d}_{mS}	Mean small bubble diameter (Table 2), m
d_o	Orifice / inner needle diameter of the gas sparger, m
\bar{d}_t	Bubble diameter at turbulent churn flow, m
$Eöd_m$	Eötvös number based on the mean bubble size
$Eöd_o$	Eötvös number based on the hole/needle size of the gas sparger
e	Bubble eccentricity
f	Correction factor for the gas holdup correlations (Table 3)
f_b	Bubble formation frequency, 1/s
g	Gravitational acceleration, m/s ²
H	Column height, m
H_0	Unaerated liquid height, m
H_{meas}	Measurement height in the bubble column, m
H_p	Height of the sparger plenum, m
h	Larger diameter of the ellipsoidal bubble, m
h^*	Vertical distance from the distributor plate to reach equilibrium bubble size, m
K_d	Gas sparger coefficient depending on its structure, e.g. $K_d = 1.0$ for spider and ring spargers
l	Small diameter of the ellipsoidal bubble, m
m	Exponent indicating the dependency of the liquid circulation rate on U_g and D
N	Number of the sparger orifices or needles
N_r	First dimensionless number defined in the force balance of a bubble (Table 2)
N_μ	Secondary dimensionless number defined in the force balance of a bubble (Table 2)
n	Exponent indicating the dependency of the gas holdup on U_g at different flow regimes
n_d	Exponent in the correlation for the radial bubble size distribution (Eq. 9)
n_α	Exponent in the correlation for the radial gas holdup distribution (Eq. 16)
P_S	Saturation pressure, Pa
P_T	Total pressure, Pa

Q_{go}	Gas volumetric flow rate in the orifice, m^3/s
R	Column radius, m
$Re_{\bar{d}_i}$	Reynolds number based on the initial bubble diameter of the gas sparger
Re_{d_o}	Reynolds number based on the sparger orifices / needle diameter
$Re_{\bar{d}_m}$	Reynolds number based on the mean bubble diameter
r_{inv}	Inversion radius of the liquid velocity, m
r	Radius, m
r_o	Orifice radius of the sparger, m
S_B	Bubble surface area, m^2
Ta	Tadaki dimensionless number (Table 3)
U_{df}	Superficial gas velocity of the small bubbles, m/s
U_g	Superficial gas velocity, m/s
U_{go}	Superficial gas velocity in the orifice / needle of the gas sparger, m/s
U_l	Liquid velocity, m/s
$U_{l,\max}$	Maximum liquid velocity in the center of the bubble column, m/s
$U_{l,circ}$	Mean liquid circulation velocity, m/s
U'	Dimensionless parameter for the prediction of the gas holdup (Table 3)
u_b	Bubble rise velocity, m/s
y	Ratio of the bubble volume at the final deattachment stage to the bubble volume at the starting stage of the deattachment from sparger

Greek symbols

α_1	Empirical coefficient (Table 2)
$\overline{\alpha}_g$	Mean gas holdup
$\overline{\alpha}_{gm,trans}$	Mean gas holdup at flow regime transition
$\overline{\alpha}_{g,LB}$	Total gas holdup for small bubbles in the churn turbulent regime
$\overline{\alpha}_{g,LB}$	Total gas holdup for large bubbles in the churn turbulent regime
$\tilde{\alpha}_g$	Radial chordal average gas holdup along the column diameter
$\alpha_{g,max}$	Maximum gas holdup in the center of the bubble column
α_g	Gas holdup
α	Exponent for the hole diameter in the gas holdup correlation (Table 3)
Γ	Gas sparger parameter for the gas holdup calculation
δ_p	Pitch size of the gas sparger, m
ϕ	Specularity coefficient for the partial slip velocity condition
ξ	Dimensionless column radius, r/R
ξ_{inv}	Dimensionless column radius at the inversion point of the liquid velocity, r_{inv}/R
μ_g	Gas viscosity, $\text{kg}\cdot\text{m}/\text{s}$
μ_l	Liquid viscosity, $\text{kg}\cdot\text{m}/\text{s}$
μ_{sl}	Modified liquid viscosity containing suspended particles, $\text{kg}\cdot\text{m}/\text{s}$
ζ	Ratio of the sparger open area to the column cross-sectional area (Table 3)
ρ_g	Gas density, kg/m^3
ρ_l	Liquid density, kg/m^3
σ	Surface tension, N/m

545 **Appendix A. Example of dimensional analysis and Buckingham Π theorem**

An example of dimensional analysis and Buckingham Π theorem (Curtis et al., 1982) is given to explain the development of the empirical correlations for the hydrodynamics in bubble columns. Equation 3 is developed based on a correlation between the decisive parameters according to

$$f(\mu_l, \rho_l, \sigma, g, U_g, \bar{d}_i, d_o) = 0. \quad (\text{A.1})$$

550 The dimensions of the decisive parameters in terms of fundamental dimensions are summarized in Table A1, which are length, mass, time and temperature.

Table A1: Dimensions of the considered parameters.

Parameter	Fundamental dimensions
μ_l	$ML^{-1}T^{-1}$
ρ_l	ML^{-3}
σ	MT^{-2}
g	LT^{-2}
U_{go}	LT^{-1}
\bar{d}_i	L
d_o	L

The number of the parameters and the fundamental dimensions are 7 and 3, respectively. The equation relating the considered parameters requires (7-3) dimensionless numbers. Buckingham referred to these numbers as Π numbers, which are independent from each other. The 555 correlation is obtained as

$$\Pi_4 = f(\Pi_3, \Pi_2, \Pi_1). \quad (\text{A.2})$$

The dimensionless numbers can be considered as multiplication of m repeating parameters with an unknown exponent c and another parameter without exponent. According to the Buckingham theorem, two conditions should be considered in deriving the dimensionless numbers: First, each of the fundamental dimensions must appear in at least one of the repeating 560 parameters. Second, the repeating parameter cannot be a dimensionless parameter. Here, the parameters d_o , g and σ are chosen as the repeating parameters. Accordingly, the dimensionless numbers are

$$\Pi_1 = d_o^{c_1} g^{c_2} \sigma^{c_3} \rho_l, \quad (\text{A.3})$$

$$\Pi_2 = d_o^{c_4} g^{c_5} \sigma^{c_6} \mu_l, \quad (\text{A.4})$$

$$\Pi_3 = d_o^{c_7} g^{c_8} \sigma^{c_9} U_{go}, \quad (\text{A.5})$$

565 and

$$\Pi_4 = d_o^{c_{10}} g^{c_{11}} \sigma^{c_{12}} \bar{d}_i. \quad (\text{A.6})$$

Considering the dimensions of the parameters and all dimensionless numbers (with dimensions of $M^0 L^0 T^0$), the exponents of the parameters can be calculated according to

$$\Pi_1 = L^{c_1} (LT^{-2})^{c_2} (MT^{-2})^{c_3} (ML^{-3}) = M^0 L^0 T^0 \rightarrow c_1 = 2, c_2 = 1, c_3 = -1, \quad (\text{A.7})$$

$$\Pi_1 = \frac{\rho_l g d_o^2}{\sigma} = E \ddot{o}_{d_o}, \quad (\text{A.8})$$

$$\Pi_2 = L^{c_4}(LT^{-2})^{c_5}(MT^{-2})^{c_6}(ML^{-1}T^{-1}) = M^0L^0T^0 \rightarrow c_4 = 0.5, c_5 = 0.5, c_6 = -1, \quad (\text{A.9})$$

570

$$\Pi_2 = \frac{g^{0.5} d_o^{0.5} \mu_l}{\sigma}, \quad (\text{A.10})$$

$$\Pi_3 = L^{c_7}(LT^{-2})^{c_8}(MT^{-2})^{c_9}(LT^{-1}) = M^0L^0T^0 \rightarrow c_7 = -0.5, c_8 = -0.5, c_9 = 0, \quad (\text{A.11})$$

$$\Pi_3 = \frac{U_{go}}{g^{0.5} d_o^{0.5}}, \quad (\text{A.12})$$

$$\Pi_4 = L^{c_{10}}(LT^{-2})^{c_{11}}(MT^{-2})^{c_{12}}(L) = M^0L^0T^0 \rightarrow c_{10} = -1, c_{11} = 0, c_{12} = 0, \quad (\text{A.13})$$

and

$$\Pi_4 = \frac{\bar{d}_i}{d_o}. \quad (\text{A.14})$$

575 The multiplication of the dimensionless numbers with the desired exponents results another dimensionless number. Instead of Π_3 we use $\Pi_1 \Pi_2^{-1} \Pi_3 = \rho_l U_{go} d_o / \mu_l = Re_{d_o}$. In this study the physical properties are constant during the measurements, which means $\Pi_2 \propto d_o$. Applying Equation A.14, the dimensionless number, $\Pi_2 = \bar{d}_i / \Pi_4$, which results

$$\Pi_4 = f(\Pi_3, \frac{\bar{d}_i}{\Pi_4}, \Pi_1), \quad (\text{A.15})$$

$$\Pi_4 = f(\Pi_3, \bar{d}_i, \Pi_1), \quad (\text{A.16})$$

580

$$\bar{d}_i = d_o f\left(\frac{\rho_l U_{go} d_o}{\mu_l}, \bar{d}_i, \frac{\rho_l g d_o^2}{\sigma}\right) = d_o f(Re_{d_o}, E \ddot{o}_{d_o}), \quad (\text{A.17})$$

and

$$\bar{d}_i = b_1 d_o Re_{d_o}^{b_2} E \ddot{o}_{d_o}^{b_3}. \quad (\text{A.18})$$

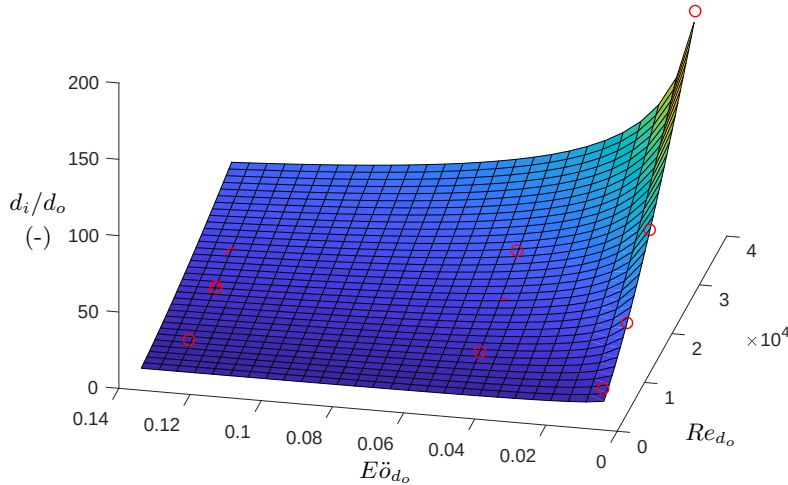


Figure A1: The 3D plot of initial bubble diameter correlation

b_1, b_2 and b_3 were obtained by applying the non-linear regression using the experimental data as

$$\bar{d}_i = 2.19 \times 10^{-9} d_o Re_{d_o}^{1.465} Edd_{d_o}^{-0.5256}. \quad (\text{A.19})$$

The 3D plot of the correlation is shown in Figure A1. The root mean square error (RMSE) and the coefficient of determination (R^2) are 3.374×10^{-3} and 0.9961, respectively.

References

- K. Akita and F. Yoshida. Gas holdup and volumetric mass transfer coefficient in bubble columns: Effects of liquid properties. *Industrial and Engineering Chemistry Process Design and Development*, 12(1):76–80, 1973.
- S. Azizi, A. Yadav, Y. Lau, U. Hampel, S. Roy, and M. Schubert. On the experimental investigation of gas-liquid flow in bubble columns using ultrafast X-ray tomography and radioactive particle tracking. *Chemical Engineering Science*, 170:320–331, 2017.
- O. M. Basha, L. Sehabiague, A. Abdel-Wahab, and B. I. Morsi. Fischer-tropsch synthesis in slurry bubble column reactors: Experimental investigations and modeling - a review. *International Journal of Chemical Reactor Engineering*, 13(3):201–288, 2015.
- A. Behkish, R. Lemoine, R. Oukaci, and B. I. Morsi. Novel correlations for gas holdup in large-scale slurry bubble column reactors operating under elevated pressures and temperatures. *Chemical Engineering Journal*, 115(3):157–171, 2006.
- S. M. Bhavaraju, R. A. Mashelkar, and H. W. Blanch. Bubble motion and mass transfer in non-Newtonian fluids: Part i. Single bubble in power law and bingham fluids. *AIChE Journal*, 24(6):1063–1070, 1978.
- A. Bieberle, D. Hoppe, E. Schleicher, and U. Hampel. Void measurement using high-resolution gamma-ray computed tomography. *Nuclear Engineering and Design*, 241(6):2086–2092, 2011.
- S. Sal, Ö. F. Güll, and M. Ozdemir. The effect of sparger geometry on gas holdup and regime transition points in a bubble column equipped with perforated plate spargers. *Chemical Engineering and Processing: Process Intensification*, 70:259–266, 2013.
- W. Curtis, J. D. Logan, and W. Parker. Dimensional analysis and the pi theorem. *Linear Algebra and its Applications*, 47:117–126, oct 1982.

- N. Deen, R. Mudde, J. Kuipers, P. Zehner, and M. Kraume. *Bubble Columns*. American Cancer Society, 2010.
- S. Degaleesan. *Fluid Dynamic Measurements and Modeling of Liquid Mixing in Bubble Columns*. PhD thesis, Washington University, 1997.
- S. Degaleesan, M. Dudukovic, and Y. Pan. Experimental study of gas-induced liquid-flow structures in bubble columns. *AICHE Journal*, 47(9):1913–1931, 2001.
- J. Dudley. Mass transfer in bubble columns: A comparison of correlations. *Water Research*, 29(4):1129–1138, 1995.
- M. P. Dudukovic and P. L. Mills. *Chemical and Catalytic Reactor Modeling*. American Chemical Society, Washington, D.C., 1984.
- F. Fischer and U. Hampel. Ultra fast electron beam X-ray computed tomography for two-phase flow measurement. *Nuclear Engineering and Design*, 240(9):2254–2259, 2010.
- F. Fischer, D. Hoppe, E. Schleicher, G. Mattausch, H. Flaske, B. R, and U. Hampel. An ultra fast electron beam x-ray tomography scanner. *Meas. Sci. Technol.*, (19), 2008.
- A. B. Gandhi, P. P. Gupta, J. B. Joshi, V. K. Jayaraman, and B. D. Kulkarni. Development of unified correlations for volumetric mass-transfer coefficient and effective interfacial area in bubble column reactors for various gas-liquid systems using support vector regression. *Industrial and Engineering Chemistry Research*, 48(9):4216–4236, 2009.
- N. W. Geary and R. G. Rice. Bubble-size prediction for rigid and flexible spargers. *AICHE Journal*, 37(2):161–168, 1991.
- M. Götz, J. Lefebvre, F. Mörs, F. Ortloff, R. Reimert, S. Bajohr, and T. Kolb. Novel gas holdup correlation for slurry bubble column reactors operated in the homogeneous regime. *Chemical Engineering Journal*, 308:1209–1224, 2017.
- H. Hikita, S. Asai, K. Tanigawa, K. Segawa, and M. Kitao. Gas hold-up in bubble columns. *Chemical Engineering Journal*, 20(1):59–67, 1980.
- N. Hooshyar, P. J. Hamersma, R. F. Mudde, and J. R. van Ommen. Intensified operation of slurry bubble columns using structured gas injection. *Canadian Journal of Chemical Engineering*, 88(4):533–542, 2010.
- G. A. Hughmark. Holdup and mass transfer in bubble columns. *Industrial Engineering Chemistry Process Design and Development*, 6:218–220, 1967.
- M. Jamialahmadi and H. Müller-Steinhagen. Effect of alcohol, organic acid and potassium chloride concentration on bubble size, bubble rise velocity and gas hold-up in bubble columns. *Chemical Engineering Journal*, 50(1):47–56, 1992.
- M. Jamialahmadi, H. Müller-Steinhagen, A. Sarrafi, and J. M. Smith. Studies of gas holdup in bubble column reactors. *Chemical Engineering and Technology*, 23(10):919–921, 2000.
- N. Kantarci, F. Borak, and K. O. Ulgen. Bubble column reactors. *Process Biochemistry*, 40(7):2263–2283, 2005.
- Y. Kawase, S. Umeno, and T. Kumagai. The prediction of gas hold-up in bubble column reactors: Newtonian and non-Newtonian fluids. *Chemical Engineering Journal*, 50(1):1–7, 1992.
- R. Krishna and J. Ellenberger. Gas holdup in bubble column reactors operating in the churn-turbulent flow regime. *AICHE Journal*, 42(9):2627–2634, 1996.
- R. Krishna, P. M. Wilkinson, and L. L. V. Dierendonck. A model for gas holdup in bubble columns incorporating the influence of gas density on flow regime transitions. *Chemical Engineering Science*, 46(10):2491–2496, 1991.

- 650 A. Kumar, T. E. Degaleesan, G. S. Laddha, and H. E. Hoelscher. Bubble swarm characteristics in bubble columns. *Canadian Journal of Chemical Engineering*, 54(5):503–508, 1976.
- S. B. Kumar, D. Moslemian, and M. P. Dudukovic. Gas-holdup measurements in bubble columns using computed tomography. *AIChE Journal*, 43(6):1414–1425, 1997.
- I. Leibson, E. G. Holcomb, A. G. Cacoso, and J. J. Jacmic. Rate of flow and mechanics of bubble formation from single submerged orifices. ii. Mechanics of bubble formation. *AIChE Journal*, 2(3):300–306, 1956.
- 655 H. Letzel, J. Schouten, R. Krishna, and C. van den Bleek. Gas holdup and mass transfer in bubble column reactors operated at elevated pressure. *Chemical Engineering Science*, 54(13-14):2237–2246, 1999.
- O. Levenspiel. *Chemical Reaction Engineering*. John Wiley & Sons, 1999.
- Y. Liao and D. Lucas. A literature review of theoretical models for drop and bubble breakup in turbulent 660 dispersions. *Chemical Engineering Science*, 64(15):3389–3406, 2009.
- Y. Liao and D. Lucas. A literature review on mechanisms and models for the coalescence process of fluid particles. *Chemical Engineering Science*, 65(10):2851–2864, 2010.
- X. Luo, D. J. Lee, R. Lau, G. Yang, and L.-S. Fan. Maximum stable bubble size and gas holdup in high-pressure slurry bubble columns. *AIChE Journal*, 45(4):665–680, 1999.
- 665 D. N. Miller. Scale-up of agitated vessels gas-liquid mass transfer. *AIChE Journal*, 20(3):445–453, 1974.
- M. Moo-Young and H. W. Blanch. Design of biochemical reactors. mass transfer criteria for simple and complex systems. In *Reactors and Reactions - Advances in Biochemical Engineering*, volume 19, pages 1–69. Springer Berlin Heidelberg, 1981.
- S. Nedeltchev and A. Schumpe. A new approach for the prediction of gas holdup in bubble columns operated 670 under various pressures in the homogeneous regime. *Journal of Chemical Engineering of Japan*, 41(8):744–755, 2008.
- R. Nottenkämper, A. Steiff, and P.-M. Weinspach. Experimental investigation of hydrodynamics of bubble columns. *German Chemical Engineering*, 6(3):147–155, 1983.
- M. Polli, M. D. Stanislao, R. Bagatin, E. A. Bakr, and M. Masi. Bubble size distribution in the sparger region 675 of bubble columns. *Chemical Engineering Science*, 57(1):197–205, 2002.
- I. G. Reilly, D. S. Scott, T. De Bruijn, A. Jain, and J. Piskorz. A correlation for gas holdup in turbulent coalescing bubble columns. *Canadian Journal of Chemical Engineering*, 64(5):705–717, 1986.
- H. P. Riquarts. Physical model for axial mixing of the liquid phase for heterogeneous flow regime in bubble columns. *German Chemical Engineering*, 4(1):18–23, 1981.
- 680 S. Roy, F. Larachi, M. H. Al-Dahhan, and M. Dudukovic. Optimal design of radioactive particle tracking experiments for flow mapping in opaque multiphase reactors. *Applied Radiation and Isotopes*, 56(3):485–503, 2002.
- R. Schafer, C. Merten, and G. Eigenberger. Bubble size distributions in a bubble column reactor under industrial conditions. *Experimental Thermal and Fluid Science*, 26(6-7):595–604, 2002.
- 685 Y. T. Shah, B. G. Kelkar, S. P. Godbole, and W. D. Deckwer. Design parameters estimations for bubble column reactors. *AIChE Journal*, 28(3):353–379, 1982.
- N. Shimada, R. Saiki, A. Dhar, K. Mizuta, and A. Tomiyama. Liquid mixing in a bubble column. *Journal of Chemical Engineering of Japan*, 45(9):632–638, 2012.
- M. Sommerfeld and D. Bröder. Analysis of hydrodynamics and microstructure in a bubble column by planar 690 shadow image velocimetry. *Industrial and Engineering Chemistry Research*, 48(1):330–340, 2009.

- H. Tsuge and S. I. Hibino. Bubble formation from a submerged single orifice accompanied by pressure fluctuations in gas chamber. *Journal of Chemical Engineering of Japan*, 11(3):173–178, 1978.
- K. Ueyama and T. Miyauchi. Properties of recirculating turbulent two phase flow in gas bubble columns. *AICHE Journal*, 25(2):258–266, 1979.
- 695 R. K. Upadhyay, H. J. Pant, and S. Roy. Liquid flow patterns in rectangular air-water bubble column investigated with radioactive particle tracking. *Chemical Engineering Science*, 96:152–164, 2013.
- J. F. Walter and H. W. Blanch. Liquid circulation patterns and their effect on gas hold-up and axial mixing in bubble columns. *Chemical Engineering Communications*, 19(4-6):243–262, 1983.
- P. M. Wilkinson and L. L. v. Dierendonck. Pressure and gas density effects on bubble break-up and gas hold-up 700 in bubble columns. *Chemical Engineering Science*, 45(8):2309–2315, 1990.
- P. M. Wilkinson, H. Haringa, and L. L. Van Dierendonck. Mass transfer and bubble size in a bubble column under pressure. *Chemical Engineering Science*, 49(9):1417–1427, 1994.
- C. Wu, K. Suddard, and M. H. Aldahhan. Bubble dynamics investigation in a slurry bubble column. *AICHE Journal*, 54(5):1203–1212, 2008.
- 705 Y. Wu and M. H. Al-Dahhan. Prediction of axial liquid velocity profile in bubble columns. *Chemical Engineering Science*, 56(3):1127–1130, 2001.
- Y. Wu, B. C. Ong, and M. H. Al-Dahhan. Predictions of radial gas holdup profiles in bubble column reactors. *Chemical Engineering Science*, 56(3):1207–1210, 2001.
- P. Zehner. Momentum, mass and heat transfer in bubble columns - 1. Flow model of the bubble column and 710 flow velocities. [Impuls-, Stoff- und Wärmetransport in Blasensäulen - 1. Strömungsmodell der Blasensäule und Flüssigkeitsgeschwindigkeiten.]. *Verfahrenstechnik*, 16(5):347–351, 1982.